Mechanical Properties
of Carbon Nanotubes

Boris I. Yakobson[1] and Phaedon Avouris[2]

[1] Center for Nanoscale Science and Technology and
   Department of Mechanical Engineering and Materials Science,
   Rice University, Houston, TX, 77251–1892, USA
   `biy@rice.edu`
[2] IBM T.J. Watson Research Center
   Yorktown Heights, NY 10598, USA
   `avouris@us.ibm.com`

Abstract. This paper presents an overview of the mechanical properties of carbon nanotubes, starting from the linear elastic parameters, nonlinear elastic instabilities and buckling, and the inelastic relaxation, yield strength and fracture mechanisms. A summary of experimental findings is followed by more detailed discussion of theoretical and computational models for the entire range of the deformation amplitudes. Non-covalent forces (supra-molecular interactions) between the nanotubes and with the substrates are also discussed, due to their significance in potential applications.

It is noteworthy that the term *resilient* was first applied not to nanotubes but to smaller fullerene cages, when Whetten *et al.* studied the high-energy collisions of C_{60}, C_{70}, and C_{84} bouncing from a solid wall of H-terminated diamond [6]. They observed no fragmentation or any irreversible atomic rearrangement in the bouncing back cages, which was somewhat surprising and indicated the ability of fullerenes to sustain great elastic distortion. The very same property of resilience becomes more significant in the case of carbon nanotubes, since their elongated shape, with the aspect ratio close to a thousand, makes the mechanical properties especially interesting and important due to potential structural applications.

1   Mechanical Properties
and Mesoscopic Duality of Nanotubes

The utility of nanotubes as the strongest or stiffest elements in nanoscale devices or composite materials remains a powerful motivation for the research in this area. While the jury is still out on practical realization of these applications, an additional incentive comes from the fundamental materials physics. There is a certain duality in the nanotubes. On one hand they have molecular size and morphology. At the same time possessing sufficient translational

symmetry to perform as very small (nano-) crystals, with a well defined primitive cell, surface, possibility of transport, etc. Moreover, in many respects they can be studied as well defined engineering structures and many properties can be discussed in traditional terms of moduli, stiffness or compliance, geometric size and shape. The mesoscopic dimensions (a nanometer scale diameter) combined with the regular, almost translation-invariant morphology along their micrometer scale lengths (unlike other polymers, usually coiled), make nanotubes a unique and attractive object of study, including the study of mechanical properties and fracture in particular.

Indeed, fracture of materials is a complex phenomenon whose theory generally requires a multiscale description involving microscopic, mesoscopic and macroscopic modeling. Numerous traditional approaches are based on a macroscopic continuum picture that provides an appropriate model except at the region of actual failure where a detailed atomistic description (involving real chemical bond breaking) is needed. Nanotubes, due to their relative simplicity and atomically precise morphology, offer us the opportunity to address the validity of different macroscopic and microscopic models of fracture and mechanical response. Contrary to crystalline solids where the structure and evolution of ever-present surfaces, grain-boundaries, and dislocations under applied stress determine the plasticity and fracture of the material, nanotubes possess simpler structure while still showing rich mechanical behavior within elastic or inelastic brittle or ductile domains. This second, theoretical-heuristic value of nanotube research supplements their importance due to anticipated practical applications. A morphological similarity of fullerenes and nanotubes to their macroscopic counterparts, geodesic domes and towers, compels one to test the laws and intuition of macro-mechanics in the scale ten orders of magnitude smaller.

In the following, Sect. 2 provides a background for the discussion of nanotubes: basic concepts from materials mechanics and definitions of the main properties. We then present briefly the experimental techniques used to measure these properties and the results obtained (Sect. 3). Theoretical models, computational techniques, and results for the elastic constants, presented in Sect. 4, are compared wherever possible with the experimental data. In theoretical discussion we proceed from linear elastic moduli to the nonlinear elastic behavior, buckling instabilities and shell model, to compressive/bending strength, and finally to the yield and failure mechanisms in tensile load. After the linear elasticity, Sect. 4.1, we outline the non-linear buckling instabilities, Sect. 4.2. Going to even further deformations, in Sect. 4.3 we discuss irreversible changes in nanotubes, which are responsible for their inelastic relaxation and failure. Fast molecular tension tests (Sect. 4.3) are followed by the theoretical analysis of relaxation and failure (Sect. 4.4), based on intramolecular dislocation failure concept and combined with the computer simulation evidence. We discuss the mechanical deformation of the nanotubes caused by their attraction to each other (supramolecular interactions) and/or to, the

substrates, Sect. 5.1. Closely related issues of manipulation of the tubes position and shape, and their self-organization into ropes and rings, caused by the seemingly weak van der Waals forces, are presented in the Sects. 5.2,5.3. Finally, a brief summary of mechanical properties is included in Sect. 6.

2 Mechanics of the Small: Common Definitions

Nanotubes are often discussed in terms of their materials applications, which makes it tempting to define "materials properties" of a nanotube itself. However, there is an inevitable ambiguity due to lack of translational invariance in the transverse directions of a singular nanotube, which is therefore not a material, but rather a structural member.

A definition of elastic moduli for a solid implies a spatial uniformity of the material, at least in an average, statistical sense. This is required for an accurate definition of any intensive characteristic, and generally fails in the nanometer scale. A single nanotube possesses no translational invariance in the radial direction, since a hollow center and a sequence of coaxial layers are well distinguished, with the interlayer spacing, c, comparable with the nanotube radius, R. It is essentially an engineering *structure*, and a definition of any material-like characteristics for a nanotube, while heuristically appealing, must always be accompanied with the specific additional assumptions involved (e.g. the definition of a cross-section area). Without it confusion can easily cripple the results or comparisons. The standard starting point for defining the elastic moduli as $1/V\ \partial^2 E/\partial\varepsilon^2$ (where E is total energy as a function of uniform strain ε) is not a reliable foothold for molecular structures. For nanotubes, this definition only works for a strain ε in the axial direction; any other deformation (e.g. uniform lateral compression) induces *non-uniform* strain of the constituent layers, which renders the previous expression misleading. Furthermore, for the hollow fullerene nanotubes, the volume V is not well defined. For a given length of a nanotube L, the cross section area A can be chosen in several relatively arbitrary ways, thus making both volume $V = LA$ and consequently the moduli ambiguous. To eliminate this problem, the intrinsic elastic energy of nanotube is better characterized by the energy change not per volume but per area S of the constituent graphitic layer (or layers), $C = 1/S\ \partial^2 E/\partial\varepsilon^2$. The two-dimensional spatial uniformity of the graphite layer ensures that $S = lL$, and thus the value of C, is unambiguous. Here l is the total circumferential length of the graphite layers in the cross section of the nanotube. Unlike more common material moduli, C has dimensionality of surface tension, N/m, and can be defined in terms of measurable characteristics of nanotube,

$$C = (1/L)\partial^2 E/\partial\varepsilon^2/\int dl \ . \tag{1}$$

The partial derivative at zero strain in all dimensions except along ε yields an analog of the elastic stiffness C_{11} in graphite, while a free-boundary (no

lateral traction on the nanotube) would correspond to the Young's modulus $Y = S_{11}^{-1}$ (S_{11} being the elastic compliance). In the latter case, the nanotube Young's modulus can be recovered and used,

$$Y = C \int dl/A , \quad \text{or} \quad Y = C/h , \tag{2}$$

but the non-unique choice of cross-section A or a thickness h must be kept in mind. For the bending stiffness K correspondingly, one has (κ being a beam curvature),

$$K \equiv (1/L)\partial^2 E/\partial \kappa^2 = C \int y^2 dl, \tag{3}$$

where the integration on the right hand side goes over the cross-section length of all the constituent layers, and y is the distance from the neutral surface. Note again, that this allows us to completely avoid the ambiguity of the mono-atomic layer "thickness", and to relate only physically measurable quantities like the nanotube energy E, the elongation ε or a curvature κ. If one adopts a particular convention for the graphene thickness h (or equivalently, the cross section of nanotube), the usual Young's modulus can be recovered, $Y = C/h$. For instance, for a bulk graphite $h = c = 0.335$ nm, $C = 342$ N/m and $Y = 1.02$ GPa, respectively. This choice works reasonably well for large diameter multiwall tubes (macro-limit), but can cause significant errors in evaluating the axial and especially bending stiffness for narrow and, in particular, single-wall nanotubes.

Strength and particularly *tensile strength* of a solid material, similarly to the elastic constants, must ultimately depend on the strength of its inter-atomic forces/bonds. However, this relationship is far less direct than in the case of linear-elastic characteristics; it is greatly affected by the particular arrangement of atoms in a periodic but imperfect lattice. Even scarce im-perfections in this arrangement play a critical role in the material nonlinear response to a large force, that is, plastic yield or brittle failure. Without it, it would be reasonable to think that a piece of material would break at $Y/8$–$Y/15$ stress, that is about 10% strain [3]. However, all single-phase solids have much lower σ_Y values, around $Y/10^4$, due to the presence of disloca-tions, stacking-faults , grain boundaries, voids, point defects, etc. The stress induces motion of the pre-existing defects, or a nucleation of the new ones in an almost perfect solid, and makes the deformation irreversible and per-manent. The level of strain where this begins to occur at a noticeable rate determines the *yield strain* ε_Y or *yield stress* σ_Y . In the case of tension this threshold reflects truly the strength of chemical-bonds, and is expected to be high for C–C based material.

A possible way to strengthen some materials is by introducing extrinsic obstacles that hinder or block the motion of dislocations [32]. There is a limit to the magnitude of strengthening that a material may benefit from, as too many obstacles will freeze (pin) the dislocations and make the solid brittle. A single-phase material with immobile dislocations or no dislocations at all

breaks in a brittle fashion, with little work required. The reason is that it is energetically more favorable for a small crack to grow and propagate. Energy dissipation due to crack propagation represents materials toughness, that is a work required to advance the crack by a unit area, $G > 2\gamma$ (which can be just above the doubled surface energy γ for a brittle material, but is several orders of magnitude greater for a ductile material like copper). Since the *c*-edge dislocations in graphite are known to have very low mobility, and are the so called *sessile* type [36], we must expect that nanotubes *per se* are brittle, unless the temperature is extremely high. Their expected high strength does not mean significant toughness, and as soon as the yield point is reached, an individual nanotube will fail quickly and with little dissipation of energy. However, in a large microstructured material, the pull-out and relative shear *between* the tubes and the matrix can dissipate a lot of energy, making the overall material (composite) toughness improved. Although detailed data is not available yet, these differences are important to keep in mind.

Compression strength is another important mechanical parameter, but its nature is completely different from the strength in tension. Usually it does not involve any bond reorganization in the atomic lattice, but is due to the buckling on the surface of a fiber or the outermost layer of nanotube. The standard measurement [37] involves the so called "loop test" where tightening of the loop abruptly changes its aspect ratio from 1.34 (elastic) to higher values when kinks develop on the compressive side of the loop. In nanotube studies, this is often called *bending strength*, and the tests are performed using an atomic force microscope (AFM) tip [74], but essentially in both cases one deals with the same intrinsic instability of a laminated structure under compression [62].

These concepts, similarly to linear elastic characteristics, should be applied to carbon and composite nanotubes with care. At the current stage of this research, nanotubes are either assumed to be structurally perfect or to contain few defects, which are also defined with atomic precision (the traditional approach of the physical chemists, for whom a molecule is a well-defined unit). A proper averaging of the "molecular" response to external forces, in order to derive meaningful material characteristics, represents a formidable task for theory. Our quantitative understanding of inelastic mechanical behavior of carbon, BN and other inorganic nanotubes is just beginning to emerge, and will be important for the assessment of their engineering potential, as well as a tractable example of the physics of fracture.

3   Experimental Observations

There is a growing body of experimental evidence indicating that carbon nanotubes (both MWNT and SWNT) have indeed extraordinary mechanical properties. However, the technical difficulties involved in the manipulation of

these nano-scale structures make the direct determination of their mechanical properties a rather challenging task.

## 3.1   Measurements of the Young's modulus

Nevertheless, a number of experimental measurements of the Young's modulus of nanotubes have been reported.

The first such study [71] correlated the amplitude of the thermal vibrations of the free ends of anchored nanotubes as a function of temperature with the Young's modulus. Regarding a MWNT as a hollow cylinder with a given wall thickness, one can obtain a relation between the amplitude of the tip oscillations (in the limit of small deflections), and the Young's modulus. In fact, considering the nanotube as a cylinder with the high elastic constant $c_{11} = 1.06$ TPa and the corresponding Young's modulus 1.02 TPa of graphite and using the standard beam deflection formula one can calculate the bending of the nanotube under applied external force. In this case, the deflection of a cantilever beam of length L with a force F exerted at its free end is given by $\delta = FL^3/(3YI)$, where I is the moment of inertia. The basic idea behind the technique of measuring free-standing room-temperature vibrations in a TEM, is to consider the limit of small amplitudes in the motion of a vibrating cantilever, governed by the well known fourth-order wave equation, $y_{tt} = -(YI/\varrho A)y_{xxxx}$, where A is the cross sectional area, and ϱ is the density of the rod material. For a clamped rod the boundary conditions are such that the function and its first derivative are zero at the origin and the second and third derivative are zero at the end of the rod. Thermal nanotube vibrations are essentially elastic relaxed phonons in equilibrium with the environment; therefore the amplitude of vibration changes stochastically with time. This stochastic driven oscillator model is solved in [38] to more accurately analyze the experimental results in terms of the Gaussian vibrational-profile with a standard deviation given by

$$\sigma^2 = \sum_{n=0}^{\infty} \sigma_n^2 = 0.4243 \frac{L^3 kT}{Y(D_o^4 - D_i^4)} \ , \tag{4}$$

with D_o and D_i the outer and inner radii, T the temperature and σ_n the standard deviation. An important assumption is that the nanotube is uniform along its length. Therefore, the method works best on the straight, clean nanotubes. Then, by plotting the mean-square vibration amplitude as a function of temperature one can get the value of the Young's modulus.

This technique was first used in [71] to measure the Young's modulus of carbon nanotubes. The amplitude of those oscillations was defined by means of careful TEM observations of a number of nanotubes. The authors obtained an average value of 1.8 TPa for the Young's modulus, though there was significant scatter in the data (from 0.4 to 4.15 TPa for individual tubes). Although this number is subject to large error bars, it is nevertheless indicative of the exceptional axial stiffness of these materials. More recently studies
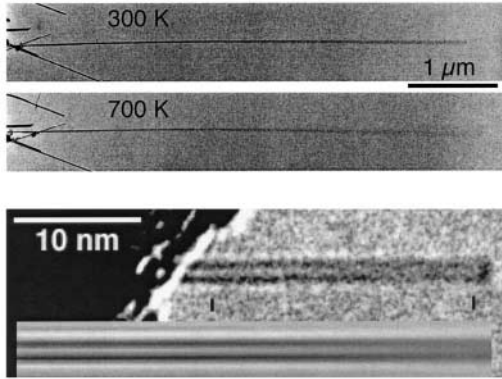
Fig. 1. *Top panel:* bright field TEM images of free-standing multi-wall carbon nano-tubes showing the blurring of the tips due to thermal vibration, from 300 to 600 K. Detailed measurement of the vibration amplitude is used to estimate the stiffness of the nanotube beam [71]. *Bottom panel:* micrograph of single-wall nanotube at room temperature, with the inserted simulated image corresponding to the best-squares fit adjusting the tube length L, diameter d and vibration amplitude (in this example, $L = 36.8$ nm, $d = 1.5$ nm, $\sigma = 0.33$ nm, and $Y = 1.33 \pm 0.2$ TPa) [38]

on SWNT's using the same technique have been reported, Fig. 1 [38]. A larger sample of nanotubes was used, and a somewhat smaller average value was obtained, $Y = 1.25 - 0.35/+0.45$ TPa, around the expected value for graphite along the basal plane. The technique has also been used in [14] to estimate the Young's modulus for BN nanotubes. The results indicate that these com-posite tubes are also exceptionally stiff, having a value of Y around 1.22 TPa, very close to the value obtained for carbon nanotubes.

Another way to probe the mechanical properties of nanotubes is to use the tip of an AFM (atomic force microscope) to bend anchored CNT's while simultaneously recording the force exerted by the tube as a function of the displacement from its equilibrium position. This allows one to extract the Young's modulus of the nanotube, and based on such measurements [74] have reported a mean value of 1.28±0.5 TPa with no dependence on tube diameter for MWNT, in agreement with the previous experimental results. Also [60] used a similar idea, which consists of depositing MWNT's or SWNT's bundled in ropes on a polished aluminum ultra-filtration membrane. Many tubes are then found to lie across the holes present in the membrane, with a fraction of their length suspended. Attractive interactions between the nanotubes and the membrane clamp the tubes to the substrate. The tip of an AFM is then used to exert a load on the suspended length of the nanotube, measuring at the same time the nanotube deflection. To minimize the uncertainty of the applied force, they calibrated the spring constant of each AFM tip (usually 0.1 N/m) by measuring its resonant frequency. The slope of the deflection versus force curve gives directly the Young's modulus for a known length and

tube radius. In this way, the mean value of the Young's modulus obtained for arc-grown carbon nanotubes was 0.81 ± 0.41 TPa. (The same study applied to disordered nanotubes obtained by the catalytic decomposition of acetylene gave values between 10 to 50 GPa. This result is likely due to the higher density of structural defects present in these nanotubes.) In the case of ropes, the analysis allows the separation of the contribution of shear between the constituent SWNT's (evaluated to be close to $G = 1$ GPa) and the tensile modulus, close to 1 TPa for the individual tubes. A similar procedure has also been used [48] with an AFM to record the profile of a MWNT lying across an electrode array. The attractive substrate-nanotube force was approximated by a van der Waals attraction similar to the carbon–graphite interaction but taking into account the different dielectric constant of the SiO$_2$ substrate; the Poisson ratio of 0.16 is taken from *ab initio* calculations. With these approximations the Young modulus of the MWNT was estimated to be in the order of 1 TPa, in good accordance with the other experimental results.

An alternative method of measuring the elastic bending modulus of nanotubes as a function of diameter has been presented by *Poncharal* et al. [52]. The new technique was based on a resonant electrostatic deflection of a multiwall carbon nanotube under an external ac-field. The idea was to apply a time-dependent voltage to the nanotube adjusting the frequency of the source to resonantly excite the vibration of the bending modes of the nanotube, and to relate the frequencies of these modes directly to the Young modulus of the sample. For small diameter tubes this modulus is about 1 TPa, in good agreement with the other reports. However, this modulus is shown to decrease by one order of magnitude when the nanotube diameter increases (from 8 to 40 nm). This decrease must be related to the emergence of a different bending mode for the nanotube. In fact, this corresponds to a wave-like distortion of the inner side of the bent nanotube. This is clearly shown in Fig. 2. The amplitude of the wave-like distortion increases uniformly from essentially zero for layers close to the nanotube center to about 2–3 nm for the outer layers without any evidence of discontinuity or defects. The non-linear behavior is discussed in more detail in the next section and has been observed in a static rather than dynamic version by many authors in different contexts [19,34,41,58].

Although the experimental data on elastic modulus are not very uniform, overall the results correspond to the values of in-plane rigidity (2) $C = 340 - 440$ N/m, that is to the values $Y = 1.0 - 1.3$ GPa for multiwall tubules, and to $Y = 4C/d = (1.36 - 1.76)$ TPa nm/d for SWNT's of diameter d.

3.2   Evidence of Nonlinear Mechanics and Resilience of Nanotubes

Large amplitude deformations, beyond the Hookean behavior, reveal nonlinear properties of nanotubes, unusual for other molecules or for the graphite fibers. Both experimental evidence and theory-simulations suggest the ability
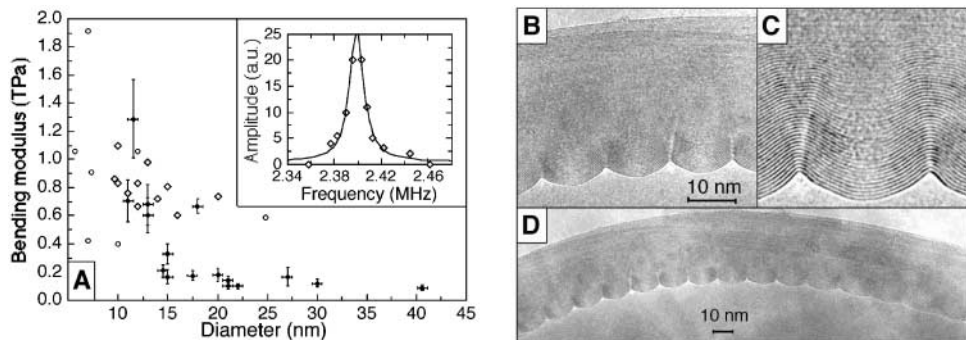
Fig. 2. A: bending modulus Y for MWNT as a function of diameter measured by the resonant response of the nanotube to an alternating applied potential (the *inset* shows the Lorentzian line-shape of the resonance). The dramatic drop in Y value is attributed to the onset of a wave-like distortion for thicker nanotubes. D: high-resolution TEM of a bent nanotube with a curvature radius of 400 nm exhibiting a wave-like distortion. B,C: the magnified views of a portion of D [52]

of nanotubes to significantly change their shape, accommodating to external forces without irreversible atomic rearrangements. They develop kinks or ripples (multiwalled tubes) in compression and bending, flatten into deflated ribbons under torsion, and still can reversibly restore their original shape. This resilience is unexpected for a graphite-like material, although folding of the mono-atomic graphitic sheets has been observed [22]. It must be attributed to the small dimension of the tubules, which leaves no room for the stress-concentrators — micro-cracks or dislocation failure piles (cf. Sect. 4.4), making a macroscopic material prone to failure. A variety of experimental evidence confirms that nanotubes can sustain significant nonlinear elastic deformations. However, observations in the nonlinear domain rarely could directly yield a measurement of the threshold stress or the force magnitudes. The facts are mostly limited to geometrical data obtained with high-resolution imaging.

An early observation of noticeable flattening of the walls in a close contact of two MWNT has been attributed to van der Walls forces pressing the cylinders to each other [59]. Similarly, a crystal-array [68] of parallel nanotubes will flatten at the lines of contact between them so as to maximize the attractive van der Waals intertube interaction (see Sect. 5.1). Collapsed forms of the nanotube ("nanoribbons"), also caused by van der Waals attraction, have been observed in experiment (Fig. 3d), and their stability can be explained by the competition between the van der Waals and elastic energies (see Sect. 5.1).

Graphically more striking evidence of resilience is provided by bent structures [19,34], Fig. 4. The bending seems fully reversible up to very large bending angles, despite the occurrence of kinks and highly strained tubule regions
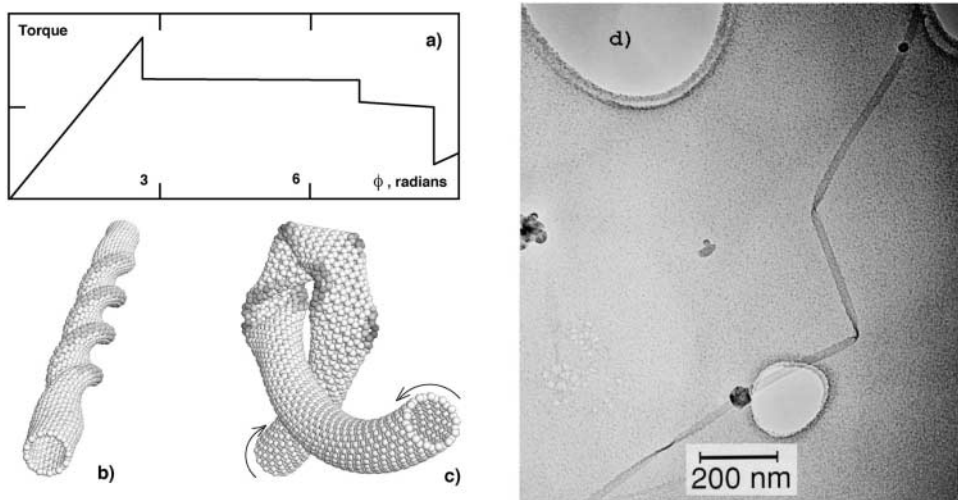
Fig. 3. Simulation of torsion and collapse [76]. The strain energy of a 25 nm long $(13, 0)$ tube as a function of torsion angle f (**a**). At the first bifurcation the cylinder flattens into a straight spiral (**b**) and then the entire helix buckles sideways, and coils in a forced tertiary structure (**c**). Collapsed tube (**d**) as observed in experiment [13]

in simulations, which are in excellent morphological agreement with the experimental images [34]. This apparent flexibility stems from the ability of the sp^2 network to rehybridize when deformed out of plane, the degree of sp^2–sp^3 rehybridization being proportional to the local curvature [27]. The accumulated evidence thus suggests that the strength of the carbon–carbon bond does not guarantee resistance to radial, normal to the graphene plane deformations. In fact, the graphitic sheets of the nanotubes, or of a plane graphite [33] though difficult to stretch are easy to bend and to deform.

A measurement with the Atomic Force Microscope (AFM) tip detects the "failure" of a multiwall tubule in bending [74], which essentially represents nonlinear buckling on the compressive side of the bent tube. The measured local stress is 15–28 GPa, very close to the calculated value [62,79]. Buckling and rippling of the outermost layers in a dynamic resonant bending has been directly observed and is responsible for the apparent softening of MWNT of larger diameters. A variety of largely and reversibly distorted (estimated up to 15% of local strain) configurations of the nanotubes has been achieved with AFM tip [23,30]. The ability of nanotubes to "survive the crash" during the impact with the sample/substrate reported in [17] also documents their ability to reversibly undergo large nonlinear deformations.
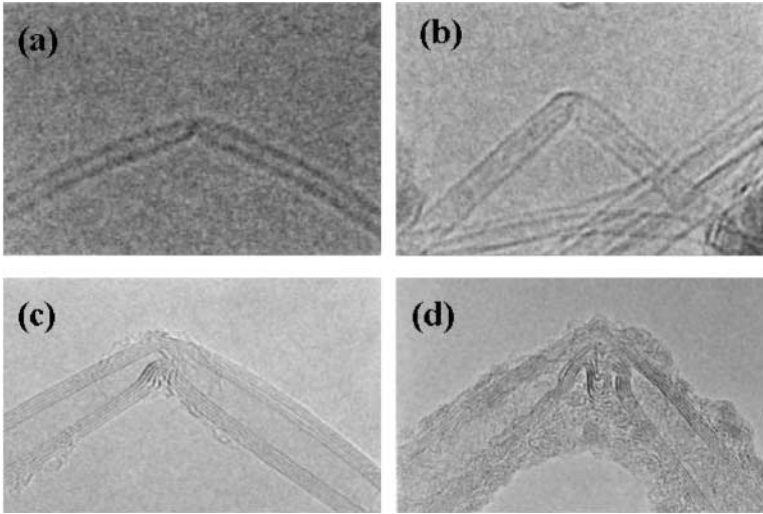
Fig. 4. HREM images of bent nanotubes under mechanical duress. (**a**) and (**b**) single kinks in the middle of SWNT with diameters of 0.8 and 1.2 nm, respectively. (**c**) and (**d**) MWNT of about 8nm diameter showing a single and a two-kink complex, respectively [34]

3.3   Attempts of Strength Measurements

Reports on measurements of carbon nanotube strength are scarce, and remain the subject of continuing effort. A nanotube is too small to be pulled apart with standard tension devices, and too strong for tiny "optical tweezers", for example. The proper instruments are still to be built, or experimentalists should wait until longer nanotubes are grown.

A bending strength of the MWNT has been reliably measured with the AFM tip [74], but this kind of failure is due to buckling of graphene layers, not the C–C bond rearrangement. Accordingly, the detected strength, up to 28.5 GPa, is two times lower than 53.4 GPa observed for non-laminated SiC nanorods in the same series of experiments. Another group [23] estimates the maximum sustained tensile strain on the outside surface of a bent tubule as large as 16%, which (with any of the commonly accepted values of the Young's modulus) corresponds to 100–150 GPa stress. On the other hand, some residual deformation that follows such large strain can be an evidence of the beginning of yield and the 5/7-defects nucleation. A detailed study of the failure via buckling and collapse of matrix-embedded carbon nanotube must be mentioned here [41], although again these compressive failure mechanisms are essentially different from the bond-breaking yield processes in tension (as discussed in Sects. 4.3,4.4).

Actual tensile load can be applied to the nanotube immersed in matrix materials, provided the adhesion is sufficiently good. Such experiments, with

stress-induced fragmentation of carbon nanotube in a polymer matrix has been reported, and an estimated strength of the tubes is 45 GPa, based on a simple isostrain model of the carbon nanotube-matrix. It has also to be remembered that the authors [72] interpret the contrast bands in HRTEM images as the locations of failure, although the imaging of the carbon nanotube through the polymer film limits the resolution in these experiments.

While a singular single-wall nanotube is an extremely difficult object for mechanical tests due to its small molecular dimensions, the measurement of the "true" strength of SWNTs in a rope-bundle arrangement is further complicated by the weakness of inter-tubular lateral adhesion. External load is likely to be applied to the outermost tubules in the bundle, and its transfer and distribution across the rope cross-section obscures the interpretation of the data. Low shear moduli in the ropes (1 GPa) indeed has been reported [60].

Recently, a suspended SWNT bundle-rope was exposed to a sideways pull by the AFM tip [73]. It was reported to sustain reversibly many cycles of elastic elongation up to 6%. If this elongation is actually transferred directly to the individual constituent tubules, the corresponding tensile strength then is above 45 GPa. This number is in agreement with that for multiwalled tubes mentioned above [72], although the details of strain distribution can not be revealed in this experiment.
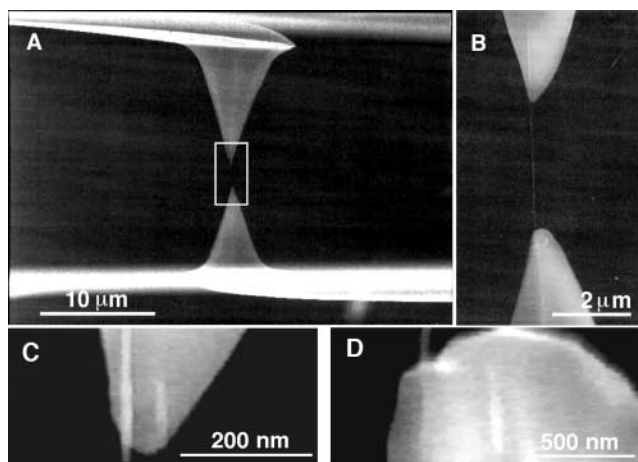
Fig. 5. A: SEM image of two oppositely aligned AFM tips holding a MWCNT which is attached at both ends on the AFM silicon tip surface by electron beam deposition of carbonaceous material. The lower AFM tip in the image is on a soft cantilever whose deflection is used to determine the applied force on the MWCNT. B–D: Large magnification SEM image of the indicated region in (A) and the weld of the MWCNT on the top AFM tip [84]

A direct tensile, rather than sideways, pull of a multiwall tube or a rope has a clear advantage due to simpler load distribution, and an important step in this direction has been recently reported [84]. In this work tensile-load experiments (Fig. 5) are performed for MWNTs reporting tensile strengths in the range of 11 to 63 GPa with no apparent dependence on the outer shell diameter. The nanotube broke in the outermost layer ("sword in sheath" failure) and the analysis of the stress-strain curves (Fig. 6) indicates a Young's modulus for this layer between 270 and 950 GPa. Moreover, the measured strain at failure can be as high as 12% change in length. These high breaking strain values also agree with the evidence of stability of highly stressed graphene shells in irradiated fullerene onions [5].

In spite of significant progress in experiments on the strength of nanotubes that have yielded important results, a direct and reliable measurement remains an important challenge for nanotechnology and materials physics.
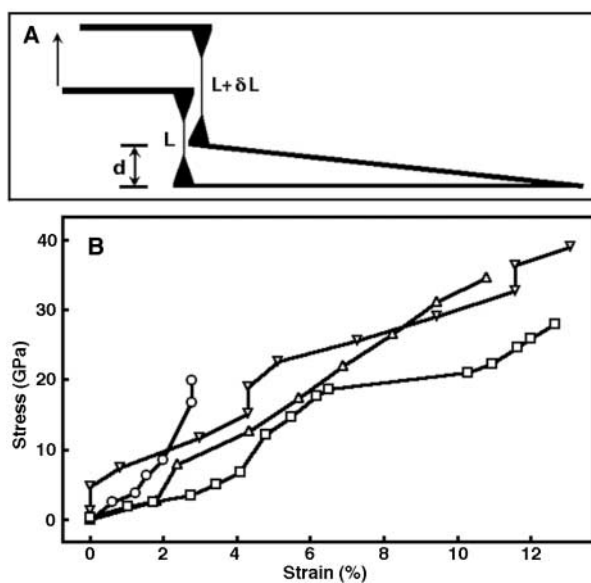
Fig. 6. A: A schematic explaining the principle of the tensile-loading experiment. B: Plot of stress versus strain curves for individual MWCNTs [84]

## 4   Theoretical and Computational Models

4.1   Theoretical Results on Elastic Constants of Nanotubes

An early theoretical report based on an empirical Keating force model for a finite, capped (5,5) tube [49] could be used to estimate a Young's modulus about 5 TPa (five times stiffer than iridium). This seemingly high value is likely due to the small length and cross-section of the chosen tube (only 400 atoms and diameter $d = 0.7$ nm). In a study of structural instabilities

of SWNT at large deformations (see Sect. 4.2) the Young's modulus that had to be assigned to *the wall* was 5 TPa, in order to fit the results of molecular dynamics simulations to the continuum elasticity theory [75,76]. From the point of view of elasticity theory, the definition of the Young's modulus involves the specification of the value of the thickness h of the tube wall. In this sense, the large value of Y obtained in [75,76] is consistent with a value of $h = 0.07$ nm for the thickness of the graphene plane. It is smaller than the value used in other work [28,42,54] that simply took the value of the graphite interlayer spacing of $h = 0.34$ nm. All these results agree in the values of inherent stiffness of the graphene layer $Yh = C$, (2), which is close to the value for graphite, $C = Yh = 342$ N/m. Further, the effective moduli of a material uniformly distributed within the entire single wall nanotube cross section will be $Y_t = 4C/d$ or $Y_b = 8C/d$, that is different for axial tension or bending, thus emphasizing the arbitrariness of a "uniform material" substitution.

The moduli C for a SWNT can be extracted from the second derivative of the *ab initio* strain energy with respect to the axial strain, $d^2E/d\varepsilon^2$. Recent calculations [61] show an average value of 56 eV, and a very small variation between tubes with different radii and chirality, always within the limit of accuracy of the calculation. We therefore can conclude that the effect of curvature and chirality on the elastic properties of the graphene shell is small. Also, the results clearly show that there are no appreciable differences between this elastic constant as obtained for nanotubes and for a single graphene sheet. The *ab initio* results are also in good agreement with those obtained in [54] using Tersoff-Brenner potentials, around 59 eV/atom, with very little dependence on radius and/or chirality.

Tight-binding calculations of the stiffness of SWNTs also demonstrate that the Young modulus depends little on the tube diameter and chirality [28], in agreement with the first principles calculations mentioned above. It is predicted that carbon nanotubes have the highest modulus of all the different types of composite tubes considered: BN, BC_3, BC_2N, C_3N_4, CN [29]. Those results for the C and BN nanotubes are reproduced in the left panel of Fig. 7. The Young's modulus approaches the graphite limit for diameters of the order of 1.2 nm. The computed value of C for the wider carbon nanotubes is 430 N/m; that corresponds to 1.26 TPa Young's modulus (with $h = 0.34$ nm), in rather good agreement with the value of 1.28 TPa reported for multi-wall nanotubes [74]. Although this result is for MWNT, the similarity between SWNT is not surprising as the intra-wall C–C bonds mainly determine the moduli. From these results one can estimate the Young's modulus for two relevant geometries: (i) *multiwall* tubes, with the normal area calculated using the interlayer spacing h approximately equal to the one of graphite, and (ii) *nanorope* or *bundle* configuration of SWNTs, where the tubes form a hexagonal closed packed lattice, with a lattice constant of $(d + 0.34$ nm). The results for these two cases are presented in the right panel of Fig. 7. The MWNT
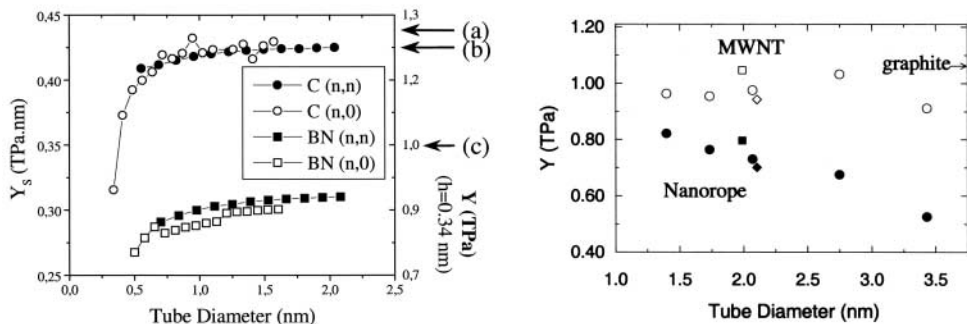
Fig. 7. *Left panel:* Young modulus for armchair and zig-zag C- and BN- nanotubes. The values are given in the proper units of TPa · nm for SWNTs (*left axis*), and converted to TPa (*right axis*) by taking a value for the graphene thickness of 0.34 nm. The experimental values for carbon nanotubes are shown on the *right-hand-side:* (**a**) 1.28 TPa [74]; (**b**) 1.25 TPa [38]; (**c**) 1 TPa for MWNT [48]. *Right panel:* Young's modulus versus tube diameter in different arrangements. *Open symbols* correspond to the multi-wall geometry (10 layer tube), and *solid symbols* for the SWNT crystalline-rope configuration. In the MWNT geometry the value of the Young's modulus does not depend on the specific number of layers (adapted from [61])

geometry gives a value that is very close to the graphitic one. The rope geometry shows a decrease of the Young's modulus with the increasing tube diameter, simply proportional to the decreasing mass-density. The computed values for MWNT and SWNT ropes are within the range of the reported experimental data, (Sect. 3.1).

Values of the Poisson ratio vary in different model computations within the range 0.15–0.28, around the value 0.19 for graphite. Since these values always enter the energy of the tube in combination with unity (5), the deviations from 0.19 are not, overall, very significant. More important is the value of another modulus, associated with the tube curvature rather than in-plane stretching. Fig. 8 shows the elastic energy of carbon and the newer composite BN and BC_3 SWNT. The energy is smaller for the composite than for the carbon tubules. This fact can be related to a small value of the elastic constants in the composite tubes as compared to graphite. From the results of Fig. 8 we clearly see that the strain energy of C, BN and BC_3 nanotubes follows the D'/d^2 law expected from linear elasticity theory, cf. (5). This dependence is satisfied quite accurately, even for tubes as narrow as $(4, 4)$. For carbon armchair tubes the constant in the strain energy equation has a value of $D' = 0.08\,eV\,nm^2/$ atom (and up to 0.09 for other chiral tubes) [61]. Previous calculations using Tersoff and Tersoff-Brenner potentials [54] predict the same dependence and give a value of $D' \sim 0.06\,eV\,nm^2/$ atom and $D' \sim 0.046\,eV\,nm^2/$ atom. The latter corresponds to the value $D = 0.85\,eV$ in the energy per area as in (5), since the area per atom is $0.0262\,nm^2$. We note in
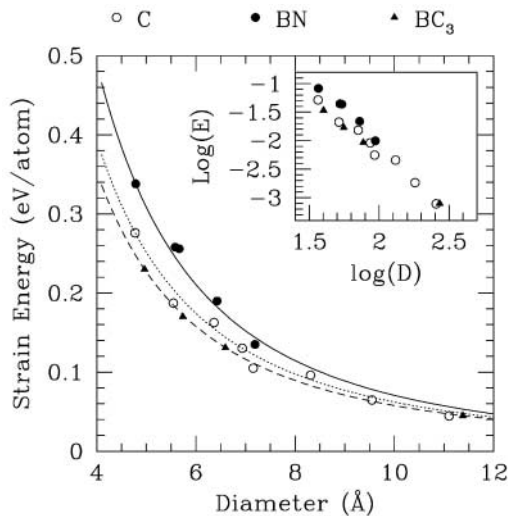
Fig. 8. Ab initio results for the total strain energy per atom as a function of the tubule diameter, d, for C- (*solid circle*), BC$_3$- (*solid triangle*) and BN-(*open circle*) tubules. The data points are fitted to the classical elastic function $1/d^2$. The *inset* shows in a log plot more clearly the $1/d^2$ dependence of the strain energy for all these tubes. We note that the elasticity picture holds down to sub-nanometer scale. The three calculations for BC$_3$ tubes correspond to the $(3,0)$, $(2,2)$ and $(4,0)$ tubes (adapted from [7,46,47,56])

Fig. 8 that the armchair (n,n) tubes are energetically more stable as compared to other chiralities with the same radius. This difference is, however, very small and decreases as the tube diameter increases. This is expected, since in the limit of large radii the same graphene value is attained, regardless of chirality. It is to some extent surprising that the predictions from elasticity theory are so similar to those of the detailed *ab initio* calculations. In [1] a complementary explanation based on microscopic arguments is provided. In a very simplified model the energetics of many different fullerene structures depend on a single structural parameter: the *planarity* ϕ_π, which is the angle formed by the π-orbitals of neighbor atoms. Assuming that the change in total energy is mainly due to the change in the nearest neighbor hopping interaction between these orbitals, and that this change is proportional to $\cos(\phi_\pi)$, the d^{-2} behavior is obtained. By using non-self-consistent first-principles calculations they have obtained a value of $D' = 0.085\,\mathrm{eV\,nm}^2/$ atom, similar to the self-consistent value given above.

4.2   Nonlinear Elastic Deformations and Shell Model

Calculations of the elastic properties of carbon nanotubes confirm that they are extremely rigid in the axial direction (high tensile) and more readily dis-

tort in the perpendicular direction (radial deformations), due to their high aspect ratio. The detailed studies, stimulated first by experimental reports of visible kinks in the molecules, lead us to conclude that, in spite of their molecular size, nanotubes obey very well the laws of continuum shell theory [2,39,70].

One of the outstanding features of fullerenes is their hollow structure, built of atoms densely packed along a closed surface that defines the overall shape. This also manifests itself in dynamic properties of molecules, which greatly resemble the macroscopic objects of continuum elasticity known as *shells*. Macroscopic shells and rods have long been of interest: the first study dates back to Euler, who discovered the elastic instability. A rod subject to longitudinal compression remains straight but shortens by some fraction ε, proportional to the force, until a critical value (Euler force) is reached. It then becomes unstable and buckles sideways at $\varepsilon > \varepsilon_{cr}$, while the force almost does not vary. For hollow tubules there is also a possibility of local buckling in addition to buckling as a whole. Therefore, more than one bifurcation can be observed, thus causing an overall nonlinear response of nanotubes to the large deforming forces (note that local mechanics of the constituent shells may well still remain within the elastic domain).

In application to fullerenes, the theory of shells now serves a useful guide [16,25,63,75,76,78], but its relevance for a covalent-bonded system of only a few atoms in diameter was far from being obvious. MD simulations seem better suited for objects that small. Perhaps the first MD-type simulation indicating the macroscopic scaling of the tubular motion emerged in the study of nonlinear resonance [65]. Soon results of detailed MD simulations for a nanotube under axial compression allowed one to introduce concepts of elasticity of shells and to adapt them to nanotubes [75,76]. MD results for other modes of load have also been compared with those suggested by the continuum model and, even more importantly, with experimental evidence [34] (see Fig. 4 in Sect. 3.2).

Figure 9 shows a simulated nanotube exposed to *axial compression*. The atomic interaction was modeled by the Tersoff-Brenner potential, which reproduces the lattice constants, binding energies, and the elastic constants of graphite and diamond. The end atoms were shifted along the axis by small steps and the whole tube was relaxed by the conjugate-gradient method while keeping the ends constrained. At small strains the total energy (Fig. 9a) grows as $E(\varepsilon) = (\frac{1}{2})E'' \cdot \varepsilon^2$, where $E'' = 59$ eV/atom. The presence of four singularities at higher strains was quite a striking feature, and the patterns (b)–(e) illustrate the corresponding morphological changes. The shading indicates strain energy per atom, equally spaced from below 0.5 eV (brightest) to above 1.5 eV (darkest). The sequence of singularities in $E(\varepsilon)$ corresponds to a loss of molecular symmetry from $D_{\infty h}$ to S_4, D_{2h}, C_{2h} and C_1. This evolution of the molecular structure can be described within the framework of continuum elasticity.
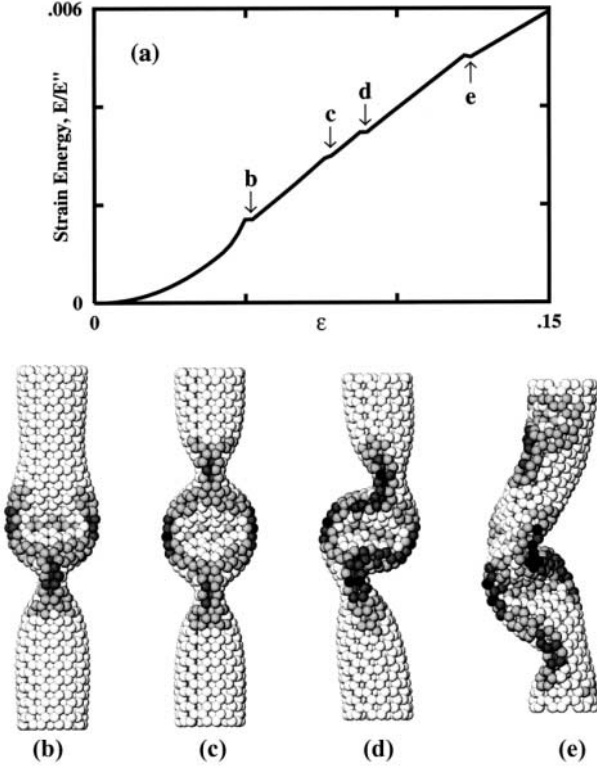
Fig. 9. Simulation of a $(7,7)$ nanotube exposed to axial compression, $L = 6\,\mathrm{nm}$. The strain energy (**a**) displays four singularities corresponding to shape changes. At $\varepsilon_c = 0.05$ the cylinder buckles into the pattern (**b**), displaying two identical flattenings, "fins", perpendicular to each other. Further increase of ε enhances this pattern gradually until at $\varepsilon_2 = 0.076$ the tube switches to a three-fin pattern (**c**), which still possesses a straight axis. In a buckling sideways at $\varepsilon_3 = 0.09$ the flattenings serve as hinges, and only a plane of symmetry is preserved (**d**). At $\varepsilon_4 = 0.13$ an entirely squashed asymmetric configuration forms (**e**) (from [75])

The intrinsic symmetry of a graphite sheet is hexagonal, and the elastic properties of two-dimensional hexagonal structures are isotropic. A curved sheet can also be approximated by a uniform shell with only two elastic parameters: flexural rigidity D, and its resistance to an in-plane stretching, the in-plane stiffness C. The energy of a shell is given by a surface integral of the quadratic form of local deformation,

$$
\begin{aligned}
E = \frac{1}{2} \int \int \{ & D[(\kappa_x + \kappa_y)^2 - 2(1-\nu)(\kappa_x \kappa_y - \kappa_{xy}^2)] \\
& + \frac{C}{(1-\nu^2)}[(\varepsilon_x + \varepsilon_y)^2 - 2(1-\nu)(\varepsilon_x \varepsilon_y - \varepsilon_{xy}^2)]\} dS,
\end{aligned}
\tag{5}
$$

where κ is the curvature variation, ε is the in-plane strain, and x and y are local coordinates). In order to adapt this formalism to a graphitic tubule, the values of D and C are identified by comparison with the detailed *ab initio* and semi-empirical studies of nanotube energetics at small strains [1,54]. Indeed, the second derivative of total energy with respect to axial strain corresponds to the in-plane rigidity C (cf. Sect. 3.1). Similarly, the strain energy as a function of tube diameter d corresponds to $2D/d^2$ in (5). Using the data of [54], one obtains $C = 59$ eV/atom $= 360$ J/m^2, and $D = 0.88$ eV. The Poisson ratio $\nu = 0.19$ was extracted from a reduction of the diameter of a tube stretched in simulations. A similar value is obtained from experimental elastic constants of single crystal graphite [36]. One can make a further step towards a more tangible picture of a tube as having wall thickness h and Young's modulus Y_s. Using the standard relations $D = Yh^3/12(1 - \nu^2)$ and $C = Y_sh$, one finds $Y_s = 5.5$ TPa and $h = 0.067$ nm. With these parameters, linear stability analysis [39,70] allows one to assess the nanotube behavior under strain.

To illustrate the efficiency of the shell model, consider briefly the case of imposed axial compression. A trial perturbation of a cylinder has a form of Fourier harmonics, with M azimuthal lobes and N half-waves along the tube (Fig. 10, inset), i.e. sines and cosines of arguments $2My/d$ and $N\pi x/L$. At a critical level of the imposed strain, $\varepsilon_c(M, N)$, the energy variation (4.1) vanishes for this shape disturbance. The cylinder becomes unstable and lowers its energy by assuming an (M, N)-pattern. For tubes of $d = 1$ nm with the shell parameters identified above, the critical strain is shown in Fig. 10. According to these plots, for a tube with $L > 10$ nm the bifurcation is first attained for $M = 1, N = 1$. The tube preserves its circular cross section and
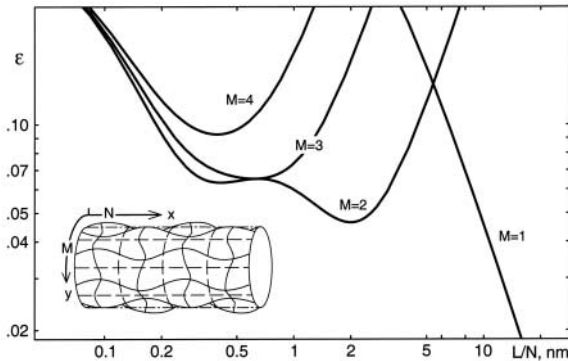
Fig. 10. The critical strain levels for a continuous, 1 nm wide shell-tube as a function of its scaled length L/N. A buckling pattern (M, N) is defined by the number of half-waves $2M$ and N in y and x directions, respectively, e.g., a $(4, 4)$-pattern is shown in the *inset*. The effective moduli and thickness are fit to graphene (from [75])

buckles sideways as a whole; the critical strain is close to that for a simple
rod,

$$\varepsilon_c = 1/2(\pi d/L)^2 \,, \tag{6}$$

or four times less for a tube with hinged (unclamped) ends. For a shorter
tube the situation is different. The lowest critical strain occurs for $M = 2$ (and $N \geq 1$, see Fig. 10), with a few separated flattenings in directions
perpendicular to each other, while the axis remains straight. For such a local
buckling, in contrast to (6), the critical strain depends little on length and
estimates to $\varepsilon_c = 4\sqrt{D/C}\ d^{-1} = (2/\sqrt{3})(1 - \nu^2)^{-1/2}\ hd^{-1}$ in the so-called
Lorenz limit. For a nanotube one finds,

$$\varepsilon_c = 0.077 \text{ nm}/d \,. \tag{7}$$

Specifically, for the 1 nm wide tube of length $L = 6$ nm, the lowest critical
strains occur for the $M = 2$ and $N = 2$ or 3 (Fig. 10), and are close to
the value obtained in MD simulations, (Fig. 9a). This is in accord with the
two- and three-fin patterns seen in Figs. 9b,c. Higher singularities cannot be
quantified by the linear analysis, but they look like a sideways beam buckling,
which at this stage becomes a non-uniform object.

Axially compressed tubes of greater length and/or tubes simulated with
hinged ends (equivalent to a doubled length) first buckle sideways as a whole
at a strain consistent with (6). After that the compression at the ends results
in bending and a local buckling inward. This illustrates the importance of
the "beam-bending" mode, the softest for a long molecule and most likely
to attain significant amplitudes due to either thermal vibrations or environ-
mental forces. In simulations of *bending*, a torque rather than force is applied
at the ends and the bending angle θ increases stepwise. While a notch in
the energy plot can be mistaken for numerical noise, its derivative $dE/d\theta$
drops significantly, which unambiguously shows an increase in tube compli-
ance — a signature of a buckling event. In bending, only one side of a tube
is compressed and thus can buckle. Assuming that it buckles when its local
strain, $\varepsilon = K \cdot (d/2)$, where K is the local curvature, is close to that in axial
compression, (7), we estimate the critical curvature as

$$K_c = 0.155 \text{ nm}/d^2 \,. \tag{8}$$

This is in excellent agreement (within 4%) with extensive simulations of single
wall tubes of various diameters, helicities and lengths [34]. Due to the end
effects, the average curvature is less than the local one and the simulated
segment buckles somewhat earlier than at $\theta_c = K_c L$, which is accurate for
longer tubes.

In simulations of *torsion*, the increase of azimuthal angle ϕ between the
tube ends results in energy and morphology changes shown in Fig. 3. In the
continuum model, the analysis based on (5) is similar to that outlined above,

except that it involves skew harmonics of arguments like $N\pi x/L \pm 2My/d$. For overall beam-buckling ($M = 1$),

$$\phi_c = 2(1+\nu)\pi \qquad\qquad (9)$$

and for the cylinder-helix flattening ($M = 2$),

$$\phi_c = 0.055 \text{ nm}^{3/2} \ L/d^{5/2} \ . \qquad\qquad (10)$$

The latter should occur first for $L < 136 \ d^{5/2}$ nm, which is true for all tubes we simulated. However, in simulations it occurs later than predicted by (10). The ends, kept circular in simulation, which is physically justifiable, by a presence of rigid caps on normally closed ends of a molecule, deter the through flattening necessary for the helix to form (unlike the local flattening in the case of an axial load).

In the above discussion, the specific values of the parameters C and D (or Y and h) are chosen to achieve the best correspondence between the elastic-shell and the MD simulation *within the same study*, performed with the Tersoff-Brenner potential. Independent studies of nanotube dynamics under compression generally agree very well with the above description, although they reveal reasonable deviations in the parameter values [16,25]. More accurate and realistic values can be derived from the TB or the *ab initio* calculations [1,7,57] of the elastic shell, and can be summarized in the somewhat "softer but thicker" shell [76]. Based on a most recent study [28] one obtains effective shell parameters $C = 415$ J/m^2 and $D = 1.6$ eV $= 2.6 \times 10^{-19}$ J, that is correspondingly $Y_s = 4.6$ TPa and $h = 0.09$ nm, cf. Sect. 4.1.

Simulations of nanotubes under mechanical duress lead to shapes very different in appearance. At the same time there are robust traits in common: a deformation, proportional to the force within Hooke's law, eventually leads to a collapse of the cylinder and an abrupt change in pattern, or a sequence of such events. The presence of a snap-through buckling of nanotubes allows for a possibility of "shape memory", when in an unloading cycle the switch between patterns occurs at a somewhat lower level of strain. A small hysteresis observed in simulations is practically eliminated by thermal motion at any finite temperature. However, this hysteresis is greatly enhanced by the presence of van der Waals attraction which causes the tube walls to "stick"-flatten together after the collapse, Fig. 3d [13]. The simulations at even a low temperature (e.g. 50 K) shows strongly enhanced thermal vibrations in the vicinity of every pattern switch, while before and after the transition only barely noticeable ripples are seen. Physically, this indicates softening of the system, when one of the eigenvalues tends to zero in the vicinity of the bifurcation.

While several reports focus on a nonlinear dynamics of an open-end SWNT, when the terminal ring atoms are displaced gradually in simulation, a more realistic interaction of a cap-closed SWNT with the (diamond or graphite) substrates has been studied recently [25]. An inward cap collapse

and/or sideways sliding of the nanotube tip along the substrate are observed, in addition to the buckling of the tubule itself. Furthermore, an interaction of a small (four SWNT) bundle and a double-wall tubule with the substrates has been also reported [26].

An atomistic modeling of multi-layer tubes remains expensive. It makes extrapolation of the continuum model tempting, but involves an interlayer van der Waals interaction. The flexural rigidity scales as $\sim h^3$ in case of a coherent, and as $\sim h$ for an incoherent stack of layers sliding with respect to each other when the tube is deformed; this affects the mechanical properties and still has to be investigated.

Direct simulations of the tubules under hydrostatic pressure have not been reported to the best of our knowledge. In this scale anisotropic lateral forces in a molecular crystal packing are more plausible than a uniform pressure. An ability of a shell-tubule to bifurcate in a flattened form makes it an example of a two-level system, which manifests in the phase-transition behavior of SWNT crystal, as was first described in [68] and is now indicated by several experimental reports. While the faceting in the triangular crystal packing results in a partial wall flattening, a singular tubule under hydrostatic pressure can collapse completely. One can resort to continuum elasticity and estimate a pressure leading to an inward buckling as $p_c = 2Y(h/d)^3$, that is thousands of atmospheres for a nanometer tube. However, it drops fast with the diameter and is assisted by a flattening effects of twisting or bending and by van der Waals attraction between the opposite walls [13]. Such collapse cannot occur simultaneously throughout the significant SWNT length, but rather propagates at a certain speed depending on the ambient over-pressure $u \propto \sqrt{(p - p_c)}$. This pressure dependence [76] is similar to the observations on macroscopic objects like underwater pipelines [50].

4.3   Atomistics of High Strain-Rate Failure

The simulations of compression, torsion, and tension described above (Sect. 4.2) do not show any bond breaking or atoms switching their positions, in spite of the very large local strain in the nanotubes. This supports the study of *axial tension*, where no shape transformations occur up to an extreme dilation. How strong in tension is a carbon nanotube? Since the tensile load does not lead to any shell-type instabilities, it is transferred more directly to the chemical bond network. The inherent strength of the carbon-carbon bond indicates that the tensile strength of carbon nanotubes might exceed that of other known fibers. Experimental measurements remain complex (Sect. 3.3) due to the small size of the grown single tubes. In the meantime, some tests are being done in computer modeling, especially well suited to the fast strain rate [75,76,77,78]. Indeed, a simulation of an object with thousand atoms even using a classical potential interaction between atoms is usually limited to picoseconds up to nanoseconds of real physical

time. This is sufficiently long by molecular standards, as is orders of magnitude greater than the periods of intramolecular vibrations or intermolecular collision times. However, it is still much less than a normal test-time for a material, or an engineering structure. Therefore a standard MD simulation addresses a "molecular strength" of the CNT, leaving the true mechanisms of material behavior to the more subtle considerations (Sect. 4.4).

In MD simulation, the high-strain-rate test proceeds in a very peculiar manner. Fast stretching simply elongates the hexagons in the tube wall, until at the critical point an atomic disorder suddenly nucleates: one or a few C–C bonds break almost simultaneously, and the resulting "hole" in a tube wall becomes a crack precursor (see Fig. 11a). The fracture propagates very quickly along the circumference of the tube. A further stage of fracture displays an interesting feature, the formation of two or more distinct chains of atoms, $\ldots = C = C = C = \ldots$, spanning the two tube fragments, Fig. 11b. The vigorous motion (substantially above the thermal level) results in frequent collisions between the chains; they coalesce, and soon only one such chain survives. A further increase of the distance between the tube ends does not break this chain, which elongates by increasing the number of carbon atoms that pop out from both sides into the necklace. This scenario is similar to the monatomic chain unraveling suggested in field-emission exper-

a)

b)
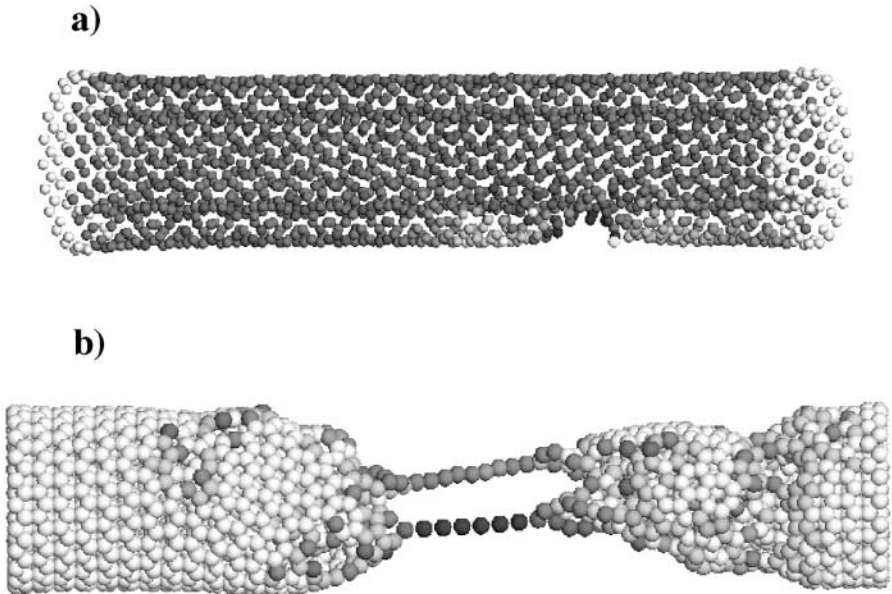
Fig. 11. High strain rate tension of a two-wall tube begins from the outermost layer, nucleating a crack precursor (**a**), where the atomic size is reduced to make the internal layer visible. Eventually it leads to the formation of monatomic chains (**b**) (from [77])

iments [53], where the electrostatic force unravels the tube like the sleeve of a sweater. Notably, the breaking strain in such fast-snap simulations is about 30%, and varies with temperature and the strain rate. (For a rope of nanotubes this translates to a more than 150 GPa breaking stress.) This high breaking strain value is consistent with the stability limit (inflection point on the energy curve) of 28% for symmetric low-temperature expansion of graphene sheet [64], and with some evidence of stability of highly stresses graphene shells in irradiated fullerene onions [5].

4.4   Yield Strength and Relaxation Mechanisms in Nanotubes

Fast strain rate (in the range of 100 MHz) simulations correspond to the elongation of the tubule at percents of the speed of sound. In contrast to such "molecular tension test", materials engineering is more concerned with the static or slow tension conditions, when the sample is loaded during significantly longer time. Fracture, of course, is a kinetic process where time is an important parameter. Even a small tension, as any non-hydrostatic stress, makes a nanotube thermodynamically meta-stable and a generation of defects energetically favorable. In order to study a slow strength-determining relaxation process, preceding the fast fracture, one should either perform extensive simulations at exceedingly elevated temperature [9,10], or apply dislocation failure theory [79,81]. It has been shown that in a crystal lattice such as the wall of a CNT, a yield to deformation must begin with a homogeneous nucleation of a slip by the shear stress present. The non-basal edge dislocations emerging in such a slip have a well-defined core, a pentagon-heptagon pair, 5/7. Therefore, the prime dipole is equivalent to the Stone–Wales (SW) defect [20] (Fig. 12). The nucleation of this prime dislocation dipole "unlocks" the nanotube for further relaxation: either brittle cleavage or a plastic flow. Remarkably, the latter corresponds to a motion of dislocations along the helical paths (glide "planes") within the nanotube wall. This causes a stepwise (quantized) necking, when the domains of different chiral symmetry and, therefore, different electronic structure are formed, thus coupling the mechanical and electrical properties [79,80]. It has further been shown [10,51,62,79,80,81,85] that the energetics of such nucleation explicitly depend on nanotube helicity.

Below, we deduce [79,81], starting with dislocation theory, the atomistics of mechanical relaxation under extreme tension. Locally, the wall of a nanotube differs little from a single graphene sheet, a two-dimensional crystal of carbon. When a uniaxial tension σ (N/m — for the two-dimensional wall it is convenient to use force per unit length of its circumference) is applied it can be represented as a sum of expansion (locally isotropic within the wall) and a shear of a magnitude $\sigma/2$ (directed at $\pm 45°$ with respect to tension). Generally, in a macroscopic crystal the shear stress relaxes by a movement of *dislocations*, the edges of the atomic extra-planes. Burgers vector $\boldsymbol{b}$ quantifies the mismatch in the lattice due to a dislocation [32]. Its glide requires only
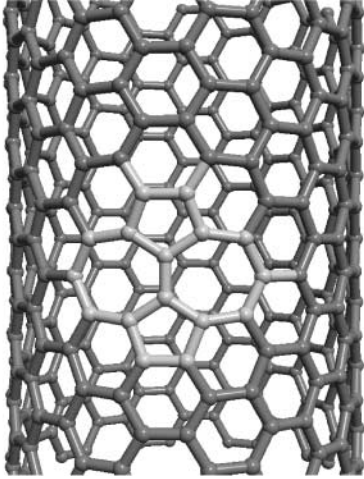
Fig. 12. Stone–Wales (SW) dipole embedded in a nanotube hexagonal wall [67]

local atomic rearrangements and presents the easiest way for strain release, provided there is sufficient thermal agitation. In an initially *perfect* lattice such as the wall of a nanotube, a yield to a great axial tension begins with a homogeneous *nucleation* of a slip, when a dipole of dislocations (a tiny loop in three-dimensional case) first has to form. The formation and further glide are driven by the reduction of the applied-stress energy, as characterized by the elastic Peach-Koehler force on a dislocation failure. The force component along $\boldsymbol{b}$ is proportional to the shear in this direction and thus depends on the angle between the Burgers vector and the circumference of the tube,

$$f_{\mathrm{b}} = -\frac{1}{2}\sigma|b|\sin 2\theta\,, \qquad\qquad (11)$$

The max $|f_{\mathrm{b}}|$ is attained on two $\pm 45°$ lines, which mark the directions of a slip in an isotropic material under tension.

The graphene wall of the nanotube is not isotropic; its hexagonal symmetry governs the three glide planes — the three lines of closest zigzag atomic packing, oriented at $120°$ to each other (corresponding to the $\{10\bar{1}\,l\}$ set of planes in three-dimensional graphite). At non-zero shear these directions are prone to slip. The corresponding c-axis edge dislocations involved in such a slip are indeed known in graphite [21,36]. The six possible Burgers vectors $1/3a\langle 2\bar{1}\bar{1}\,0\rangle$ have a magnitude $b = a = 0.246$ nm (lattice constant), and the dislocation core is identified as a 5/7 pentagon-heptagon pair in the honeycomb lattice of hexagons. Therefore, the primary nucleated dipole must have a 5/7/7/5 configuration (a 5/7 attached to an inverted 7/5 core). This configuration is obtained in the perfect lattice (or a nanotube wall) by a $90°$ rotation of a single C–C bond, well known in fullerene science as a Stone–Wales diatomic interchange [20]. One is led to conclude that the SW

transformation is equivalent to the smallest slip in a hexagonal lattice and must play a key role in the nanotube relaxation under external force.

The preferred glide is the closest to the maximum-shear $\pm 45°$ lines, and depends on how the graphene strip is rolled-up into a cylinder. This depends on nanotube helicity specified by the chiral indices (c_1, c_2) or a chiral angle θ indicating how far the circumference departs from the leading zigzag motif $\boldsymbol{a}_1$. The max $|f_b|$ is attained for the dislocations with $\boldsymbol{b} = \pm(0, 1)$ and their glide reduces the strain energy,

$$E_g = -|f_b a| = -Ca^2/2 \cdot \sin(2\theta + 60°)\varepsilon\,, \tag{12}$$

per one displacement, a. Here ε is the applied strain, and $C = Yh = 342$ N/m can be derived from the Young modulus of $Y = 1020$ GPa and the inter-layer spacing $h = 0.335$ nm in graphite; one then obtains $Ca^2/2 = 64.5$ eV. Equation (12) allows one to compare different nanotubes (assuming a similar amount of pre-existing dislocations); the more energetically favorable is the glide in a tube, the earlier it must yield to applied strain.

In a pristine nanotube-molecule, the 5/7 dislocations have first to emerge as a dipole, by a prime SW transformation. Topologically, the SW defect is equivalent to either one of the two dipoles, each formed by an $\sim a/2$ slip. Applying (11) to each of the slips one finds,

$$E_{sw} = E_o - A\varepsilon - B\sin(2\theta + 30°)\varepsilon\,. \tag{13}$$

The first two terms, the zero-strain formation energy and possible isotropic dilation, do not depend on nanotube symmetry. The symmetry-dependent third term, which can also be derived as a leading term in the Fourier series, describes the essential effect: SW rotation gains more energy in the armchair $(\theta = 30°)$ nanotube, making it the weakest, most inclined to SW nucleation of the dislocations, in contrast to the zigzag $(\theta = 0)$ where the nucleation is least favorable.

Consider, for example, a (c, c) armchair nanotube as a typical representative (we will also see below that this armchair type can undergo a more general scenario of relaxation.) The initial stress-induced SW rotation creates a geometry that can be viewed as either a dislocation dipole or a tiny crack along the equator. Once "unlocked", the SW defect can ease further relaxation. At this stage, both brittle (dislocation pile-up and crack extension), or plastic (separation of dislocations and their glide away from each other) routes are possible, the former usually at larger stress and the latter at higher temperatures [9,10,79,80,81].

Formally, both routes correspond to a further sequence of SW switches. The 90° rotation of the bonds at the "crack tip" (Fig. 13, left column) will result in a 7/8/7 flaw and then 7/8/8/7 etc. This further strains the bonds-partitions between the larger polygons, leading eventually to their breakage, with the formation of greater openings like 7/14/7 etc. If the crack, represented by this sequence, surpasses the critical Griffith size, it cleaves the tubule.
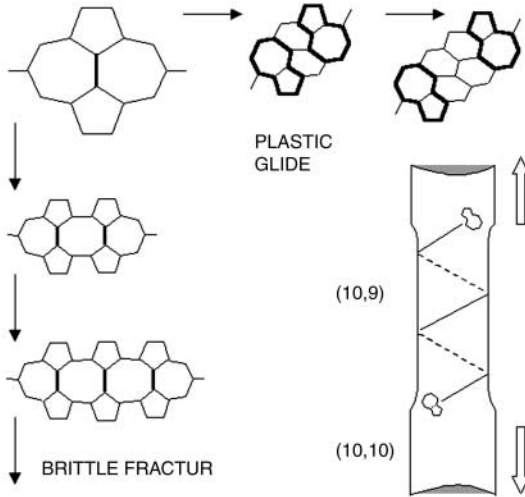
Fig. 13. SW transformations of an equatorially oriented bond into a vertical position creates a nucleus of relaxation (*top left corner*). It evolves further as either a crack (brittle fracture route, *left column*) or as a couple of dislocations gliding away along the spiral slip plane (plastic yield, *top row*). In both cases only SW rotations are required as elementary steps. The stepwise change of the nanotube diameter reflects the change of chirality (*bottom right image*) causing the corresponding variations of electrical properties [81]

In a more interesting distinct alternative, the SW rotation of another bond (Fig. 13, top row) divides the 5/7 and 7/5, as they become two dislocation cores separated by a single row of hexagons. A next similar SW switch results in a double-row separated pair of the 5/7's, and so on. This corresponds, at very high temperatures, to a plastic flow *inside* the nanotube-molecule, when the 5/7 and 7/5 twins glide away from each other driven by the elastic forces, thus reducing the total strain energy [cf. (12)]. One remarkable feature of such glide is due to mere cylindrical geometry: the glide "planes" in case of nanotubes are actually spirals, and the slow thermally-activated Brownian walk of the dislocations proceeds along these well-defined trajectories. Similarly, their extra-planes are just the rows of atoms also curved into the helices.

A nanotube with a 5/7 defect in its wall loses axial symmetry and has a bent equilibrium shape; the calculations show [12] the junction angles $< 15°$. Interestingly then, an exposure of an even achiral nanotube to the axially symmetric tension generates two 5/7 dislocations, and when the tension is removed, the tube "freezes" in an asymmetric configuration, S-shaped or C-shaped, depending on the distance of glide, that is time of exposure. Of course the symmetry is conserved statistically, since many different shapes form under identical conditions.

When the dislocations sweep a noticeable distance, they leave behind a tube segment changed strictly following the topological rules of dislocation theory. By considering a planar development of the tube segment containing a 5/7, for the new chirality vector c' one finds,

$$(c'_1, c'_2) = (c_1, c_2) - (b_1, b_2),$$ (14)

with the corresponding reduction of diameter, d. While the dislocations of the first dipole glide away, a generation of another dipole results, as shown above, in further narrowing and proportional elongation under stress, thus forming a neck. The orientation of a generated dislocation dipole is determined every time by the Burgers vector closest to the lines of maximum shear ($\pm 45°$ cross at the end-point of the current circumference-vector c). The evolution of a (c, c) tube will be: $(c, c) \rightarrow (c, c - 1) \rightarrow (c, c - 2) \rightarrow \ldots (c, 0) \rightarrow [(c - 1, 1)$ or $(c, -1)] \rightarrow (c - 1, 0) \rightarrow [(c - 2, 1)$ or $(c - 1, -1)] \rightarrow (c - 2, 0) \rightarrow [(c - 3, 1)$ or $(c - 2, -1)] \rightarrow (c - 3, 0)$ etc. It abandons the armchair (c, c) type entirely, but then oscillates in the vicinity of to be zigzag (c,0) kind, which appears a peculiar attractor. Correspondingly, the diameter for a $(10, 10)$ tube changes stepwise, $d = 1.36$, 1.29, 1.22, 1.16 nm, etc., the local stress grows in proportion and this quantized necking can be terminated by a cleave at late stages. Interestingly, such plastic flow is accompanied by the change of electronic structure of the emerging domains, governed by the vector (c_1, c_2). The armchair tubes are metallic, others are semiconducting with the different band gap values. The 5/7 pair separating two domains of different chirality has been discussed as a pure-carbon heterojunction [11,12]. It is argued to cause the current rectification detected in a nanotube nanodevice [15] and can be used to modify, in a controlled way, the electronic structure of the tube. Here we see how this electronic heterogeneity can arise from a mechanical relaxation at high temperature: if the initial tube was armchair-metallic, the plastic dilation transforms it into a semiconducting type irreversibly.

Computer simulations have provided a compelling evidence of the mechanisms discussed above. By carefully tuning the tension in the tubule and gradually elevating its temperature, with extensive periods of MD annealing, the first stages of the mechanical yield of CNT have been observed [9,10]. In simulation of tensile load the novel patterns in plasticity and breakage, just described above, clearly emerge.

Classical MD simulations have been carried out for tubes of various geometries with diameters up to 13 nm. Such simulations, although limited by the physical assumptions used in deriving the interatomic potential, are still invaluable tools in investigating very large systems in the time scales that are characteristic of fracture and plasticity phenomena. Systems containing up to 5000 atoms have been studied for simulation times of the order of nanoseconds. The ability of the classical potential to correctly reproduce the energetics of the nanotube systems has been verified through comparisons with TB and *ab initio* simulations [9,10].

Beyond a critical value of the tension, an armchair nanotube under axial tension releases its excess strain via spontaneous formation of a SW defect through the rotation of a C-C bond producing two pentagons and two heptagons, 5/7/7/5 (Fig. 14). Further, the calculations [9,10] show the energy of the defect formation, and the activation barrier, to decrease approximately linearly with the applied tension; for (10,10) tube the formation energy can be approximated as $E_{\mathrm{sw}}(\mathrm{eV}) = 2.3 - 40\varepsilon$. The appearance of a SW defect represents the nucleation of a (degenerate) dislocation loop in the planar hexagonal network of the graphite sheet. The configuration 5/7/7/5 of this primary dipole is a 5/7 core attached to an inverted 7/5 core, and each 5/7 defect can indeed further behave as a single edge dislocation in the graphitic plane. Once nucleated, the dislocation loop can split in simulations into two
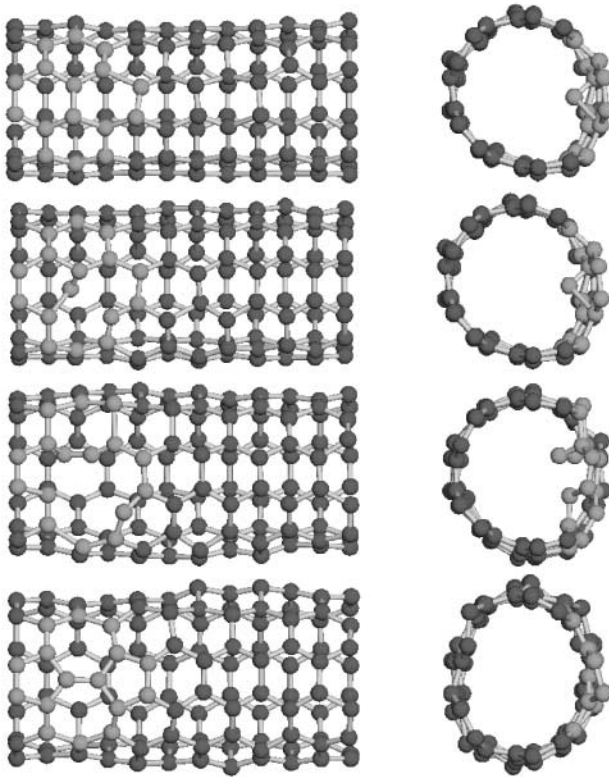
Fig. 14. Kinetic mechanism of 5/7/7/5 defect formation from an *ab-initio* quantum mechanical molecular dynamics simulation for the $(5, 5)$ tube at 1800 K [10]. The atoms that take part in the Stone–Wales transformation are in lighter gray. The four snapshots show the various stages of the defect formation, from *top to bottom:* system in the ideal configurations ($t = 0\,\mathrm{ps}$); breaking of the first bond ($t = 0.10\,\mathrm{ps}$); breaking of the second bond ($t = 0.15\,\mathrm{ps}$); the defect is formed ($t = 0.20\,\mathrm{ps}$)

dislocation cores, $5/7/7/5 \leftrightarrow 5/7 + 7/5$, which are then seen to glide through successive SW bond rotations. This corresponds to a plastic flow of dislocations and gives rise to possible ductile behavior. The thermally activated migration of the cores proceeds along the well-defined trajectories (Fig. 15) and leaves behind a tube segment changed according to the rules of dislocation theory, (14). The tube thus abandons the armchair symmetry (c, c) and undergoes a visible reduction of the diameter, a first step of the possible quantized necking in "intramolecular plasticity" [79,80,81].

The study, based on the extensive use of classical, tight-binding and ab initio MD simulations [10], shows that the different orientations of the carbon bonds with respect to the strain axis (in tubes of different symmetry) lead to different scenarios. Ductile or brittle behaviors can be observed in nanotubes of different indices under the same external conditions. Furthermore, the behavior of nanotubes under large tensile strain strongly depends on their symmetry and diameter. Several modes of behavior are identified, and a map of their ductile-vs-brittle behavior has been proposed. While graphite is brittle, carbon nanotubes can exhibit plastic or brittle behavior under deformation, depending on the external conditions and tube symmetry. In the case of a zig-zag nanotube (longitudinal tension), the formation of the SW defect is strongly dependent on curvature, i.e., on the diameter of the tube and gives rise to a wide variety of behaviors in the brittle-vs-ductile map of stress response of carbon nanotubes [10]. In particular, the formation energy of the off-axis 5/7/7/5 defect (obtained via the rotation of the C–C bond oriented 120° to the tube axis) shows a crossover with respect to the diameter.
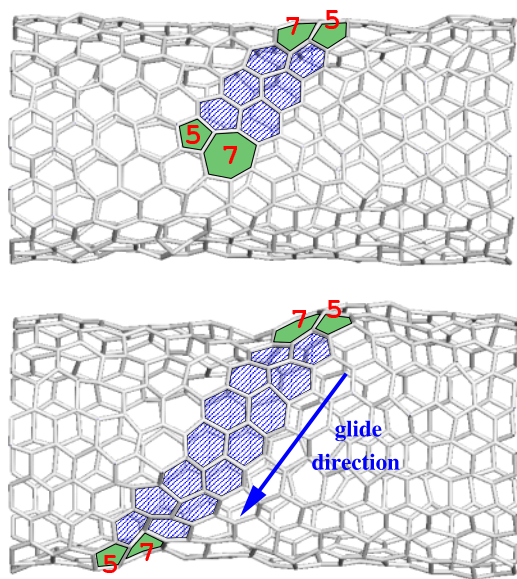
Fig. 15. Evolution of a (10,10) nanotube at $T = 3000$ K, strain 3 % within about 2.5 ns time. An emerging Stone–Wales defect splits into two 5/7 cores which migrate away from each other, each step of this motion being a single-bond rotation. The shaded area indicates the migration path of the 5/7 edge dislocation failure [9] and the resulting nanotube segment is reduced to the (10,9) in accord with (14) [80,81]

It is negative for $(c, 0)$ tubes with $c < 14$ ($d < 1.1$ nm). The effect is clearly due to the variation in curvature, which in the small-diameter tubes makes the process energetically advantageous. Therefore, above a critical value of the curvature a plastic behavior is possible and the tubes can be ductile.

Overall, after the nucleation of a first 5/7/7/5 defect in the hexagonal network either brittle cleavage or plastic flow are possible, depending on tube symmetry, applied tension and temperature. Under high strain and low temperature conditions, all tubes are brittle. If, on the contrary, external conditions favor plastic flow, such as low strain and high temperature, tubes of diameter less than approximately 1.1 nm show a completely ductile behavior, while larger tubes are moderately or completely brittle depending on their symmetry.

## 5   Supramolecular Interactions

Most of the theoretical discussions of the structure and properties of carbon nanotubes involve free unsupported nanotubes. However, in almost all experimental situations the nanotubes are supported on a solid substrate with which they interact. Similarly, nanotubes in close proximity to each other will interact and tend to associate and form larger aggregates [69,82].

5.1   Nanotube–Substrate and Nanotube–Nanotube Interactions: Binding and Distortions

These nanotube–substrate interactions can be physical or chemical. So far, however, only physical interactions have been explored. The large polarizability of carbon nanotubes (see article by S. Louie in this volume) implies that these physical interactions (primarily van der Waals forces) are significant. One very important consequence of the strong adhesive forces with which carbon nanotubes bind to a substrate is the deformation of the atomic structure of the nanotube itself. An experimental demonstration of this effect is given in Fig. 16, which shows non-contact AFM images of two pairs of overlapping multi-wall nanotubes deposited on an inert H-passivated silicon surface. The nanotubes are clearly distorted in the overlap regions with the upper nanotubes bending around the lower ones [30,31]. These distortions arise from the tendency of the upper CNTs to increase their area of contact with the substrate so as to increase their adhesion energy. Counteracting this tendency is the rise in strain energy produced from the increased curvature of the upper tubes and the distortion of the lower tube. The total energy of the system can be expressed as an integral of the strain energy $U(\kappa)$ and the adhesion energy $V(z)$ over the entire tube profile: $E = \int \{U(\kappa) + V[z(x)]dx\}$. Here, κ is the local tube curvature and $V[z(x)]$ the nanotube-substrate interaction potential at a distance z above the surface. Using the experimental value of Young's modulus for MWNTs [71,74] and by fitting to the experimentally observed nanotube profile, one can estimate the binding energy from

the observed distortion. For example, for a $100\,\text{Å}$ diameter MWNT a binding energy of about $0.8\,\text{eV/Å}$ is obtained. Therefore, van der Waals binding energies, which for individual atoms or molecules are weak (typically $0.1\,\text{eV}$), can be quite strong for mesoscopic systems such as the CNTs. High binding energies imply that strong forces are exerted by nanotubes on underlying surface features such as steps, defects, or other nanotubes. For example, the force leading to the compression of the lower tubes in Fig. 16a is estimated to be as high as 30 nN. The effect of these forces can be observed as a reduced inter-tube electrical resistance in crossed tube configurations similar to those shown in Fig. 16 [24].

The axial distortions of CNTs observed in AFM images are also found in molecular dynamics and molecular mechanics simulations. Molecular mechanics represents a simple alternative to the Born-Oppenheimer approximation-based electronic structure calculations. In this case, nuclear motion is studied assuming a fixed electron distribution associated with each atom. The molecular system is described in terms of a collection of spheres representing the atoms, which are connected with springs to their neighbors. The motion of the atoms is described classically using appropriate potential energy functions. The advantage of the approach is that very large systems (many thousands of atoms) can be easily simulated. Figure 17a,b show the results of such simulations involving two single-walled (10,10) CNTs crossing each other over a graphite slab [31]. In addition to their axial distortion, the two nanotubes develop a distorted, non-circular cross-section in the overlap region. Further results on the radial distortions of single-walled nanotubes due to van der Waals interactions with a graphite surface are shown in Fig. 17c. The adhesion forces tend to flatten the bottom of the tubes so as to increase the area of contact. At the same time, there is an increase in the curvature of the tube and therefore a rise in strain energy E_S. The resulting overall shape is again dictated by the optimization of these two opposing trends. Small diameter
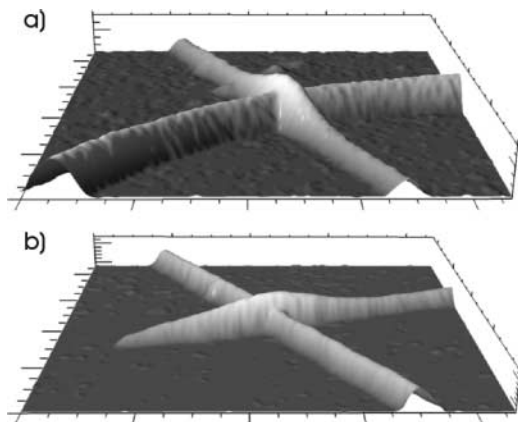
Fig. 16. AFM non-contact mode images of two overlapping multi-wall nanotubes. The *upper* tubes are seen to wrap around the *lower* ones which are slightly compressed. The size of image (**a**) is $330\,\text{nm} \times 330\,\text{nm}$ and that of (**b**) is $500\,\text{nm} \times 500\,\text{nm}$ [4]
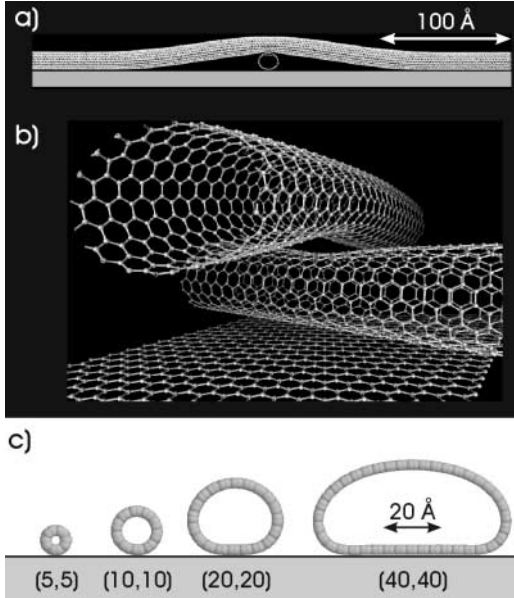
Fig. 17. Molecular mechanics calculations on the axial and radial deformation of single-wall carbon nanotubes. (**a**) Axial deformation resulting from the crossing of two (10,10) nanotubes. (**b**) Perspective close up of the same crossed tubes showing that both tubes are deformed near the contact region. (**c**) Computed radial deformations of single-wall nanotubes adsorbed on graphite [4]

tubes that already have a small radius of curvature R_C resist further distortion ($E_S \propto R_C^{-2}$), while large tubes flatten out and increase considerably their binding energy [by 115% in the case of the (40,40) tube]. In the case of MWNTs, we find that as the number of carbon shells increases, the overall gain in adhesion energy due to distortion decreases as a result of the rapidly increasing strain energy [31].

The AFM results and the molecular mechanics calculations indicate that carbon nanotubes in general tend to adjust their structure to follow the surface morphology of the substrate. One can define a critical radius of surface curvature R_{CRT} above which the nanotube can follow the surface structure or roughness. Given that the strain energy varies more strongly with tube diameter ($\propto d^4$) than the adhesion energy ($\propto d$), the critical radius is a function of the NT diameter. For example, R_{CRT} is about $(12d)^{-1}$ for a CNT with a $d = 1.3\,\mathrm{nm}$, while it is about $(50d)^{-1}$ for a CNT with $d = 10\,nm$.

5.2 Manipulation of the Position and Shape of Carbon Nanotubes

A key difference between the mechanical properties of CNTs and carbon fibers is the extraordinary flexibility and resistance to fracture of the former. Furthermore, the strong adhesion of the CNTs to their substrate can stabilize highly strained configurations. Deformed, bent and buckled nanotubes were clearly observed early in TEM images [34]. One can also mechanically manipulate and deform the CNTs using an AFM tip and then study the properties

of the deformed structures using the same instrument [23,30]. For this purpose one uses the AFM in the so-called contact mode with normal forces of the order of 10–50 nN [30]. It was found that most MWNTs can sustain multiple bendings and unbending without any observable permanent damage. Bending of MWNTs induces buckling, observed in the form of raised points along the CNT, due to the collapsing of shells. When the bending curvature is small a series of regularly spaced buckles appear on the inside wall of the nanotube [23]. This phenomenon is analogous to axial bifurcations predicted by a continuum mechanics treatment of the bending of tubes [39].

In studies of electrical or other properties of individual CNTs it is highly desirable to be able to manipulate them and place them in particular positions of the experimental setup, such as on metal electrodes in conductance studies, or in order to build prototype electronic devices structures. Again the AFM can be used for this purpose. The shear stress of CNTs on most surfaces is high, so that not only can one control the position of the nanotubes at even elevated temperatures, but also their shape.

In Fig. 18, a MWNT is manipulated in a series of steps to fabricate a simple device [4]. While highly distorted CNT configurations were formed during the manipulation process, no obvious damage was induced in the CNT. The same conclusion was reached by molecular dynamics modeling of the bending of CNTs [34]. The ability to prepare locally highly strained configurations stabilized by the interaction with the substrate, and the well known dependence of chemical reactivity on bond strain suggest that manipulation may be used to produce strained sites and make them susceptible to local chemistry. Furthermore, bending or twisting CNTs changes their electrical properties [35,55] and, in principle, this can be used to modify the electrical behavior of CNTs through mechanical deformation.

## 5.3   Self-Organization of Carbon Nanotubes: Nanotube Ropes, Rings, and Ribbons

Van der Waals forces play an important role not only in the interaction of the nanotubes with the substrate but also in their mutual interaction [68]. The different shells of a MWNT interact primarily by van der Waals forces; single-walled tubes form ropes for the same reason [69]. In these ropes the nanotubes form a regular triangular lattice. Calculations have shown that the binding forces in a rope are substantial. For example, the binding energy of 1.4 nm diameter SWNTs is estimated to be about 0.48 eV/nm, and rises to 1.8 eV/nm for 3 nm diameter tubes [68]. The same study showed that the nanotubes may be flattened at the contact areas to increase adhesion [68]. Aggregation of single-walled tubes in ropes is also expected to affect their electronic structure. When a rope is formed from metallic $(10, 10)$ nanotubes a pseudogap of the order of 0.1 eV is predicted to open up in the density of states due to the breaking of mirror symmetry in the rope [18].
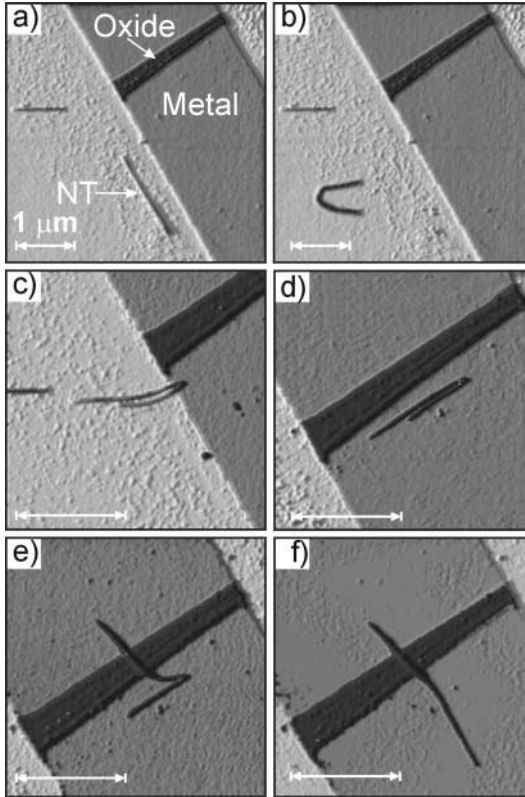
Fig. 18. AFM manipulation of a single multi-wall carbon nanotube such that electrical transport through it can be studied. Initially, the nanotube is located on the insulating (SiO₂) part of the sample. In a stepwise fashion (not all steps are shown) it is dragged up the 80 Å high metal thin film wire and finally is stretched across the oxide barrier [4]

A different manifestation of van der Waals interactions involves the self-interaction between two segments of the same single-wall CNT to produce a closed ring (loop) [44,45]. Nanotube rings were first observed in trace amounts in the products of laser ablation of graphite and were assigned a toroidal structure [40]. More recently, rings of SWNTs were synthesized with large yields (up to 50%) from straight nanotube segments, Fig. 19. These rings were shown to be coils not tori [45].

The formation of coils by CNTs is particularly intriguing. While coils of biomolecules and polymers are well known structures, they are stabilized by a number of interactions that include hydrogen bonds and ionic interactions [8]. On the other hand, the formation of nanotube coils is surprising, given the high flexural rigidity of CNTs and the fact that CNT coils can only be stabilized by van der Waals forces. However, estimates based on continuum mechanics show that in fact it is easy to compensate for the strain energy induced by the coiling process through the strong adhesion between tube segments in the coil. Figure 20 shows how a given length of nanotube l should be divided between the perimeter of the coil, $2\pi R$, that defines the strain energy and the interaction length, $l_i = l - 2\pi R$, that contributes to
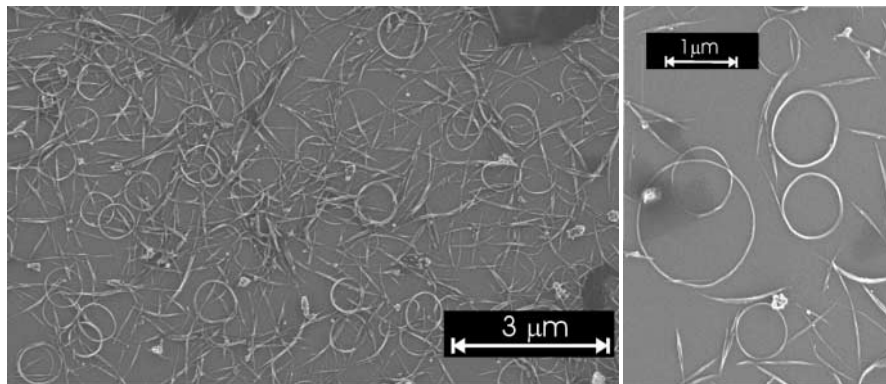
Fig. 19. Scanning electron microscope images of rings of single-wall nanotubes dispersed on hydrogen-passivated silicon substrates [45]
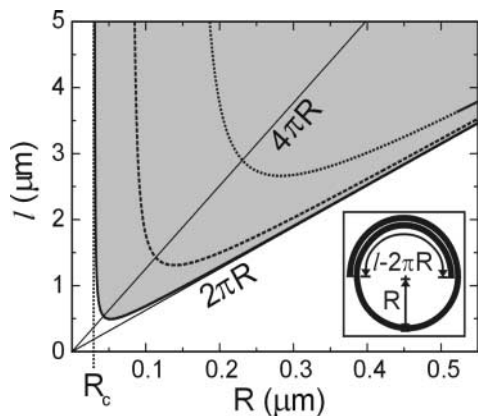
Fig. 20. Thermodynamic stability limits for rings formed by coiling single wall nanotubes with radii of 0.7 nm (plain line), 1.5 nm (dashed line), and 4.0 nm (dotted line) calculated using a continuum elastic model [45]

the adhesion (see the schematic in the inset) so that a stable structure is formed [45]. From this figure it is clear that the critical radius R_C for forming rings is small, especially for small radius CNTs such as the (10,10) tube ($r = 0.7$ nm).

The coiling process is kinetically controlled. The reason is easy to understand; to form a coil the two ends of the tube have to come first very close to each other before any stabilization (adhesion) begins to take place. This bending involves a large amount of strain energy $E_S \propto R^{-2}$, and the activation energy for coiling will be of the order of this strain energy (i.e. several eV). Similar arguments hold if, instead of a single SWNT, one starts with a SWNT rope. Experimentally, the coiling process is driven by exposure to ultrasound [44]. Ultrasonic irradiation can provide the energy for thermal activation [66], however, it is unrealistic to assume that the huge energy needed is supplied in the form of heat energy. It is far more likely that mechanical

processes associated with cavitation, i.e. the formation and collapse of small bubbles in the aqueous solvent medium that are generated by the ultrasonic waves, are responsible for tube bending [66]. The nanotubes may act as nucleation centers for bubble formation so that a hydrophobic nanotube trapped at the bubble-liquid interface is mechanically bent when the bubble collapses. Once formed, a nanotube "proto-ring" can grow thicker by the attachment of other segments of SWNTs or ropes. The synthesis of nanotube rings opens the door for the fabrication of more complex nanotube-based structures relying on a combination of mechanical manipulation and self-adhesion forces.

Finally, we note that opposite sections of the carbon atom shell of a nanotube also attract each other by van der Waals forces, and under certain conditions this attraction energy (E_{vdW}) may lead to the collapse of the nanotube to a ribbon-like structure. Indeed, such structures are often observed in TEM [13] and AFM images [43] of nanotubes (primarily multi-wall tubes). The elastic curvature energy per unit length of a tube is proportional to $1/R$ (R, radii of the tubes). However, for a fully collapsed single-wall tubule, the energy contains the higher curvature energy due to the edges, independent of the initial radius, and a negative (attractive) van der Waals contribution, $\varepsilon_{\mathrm{vdW}} \sim 0.03-0.04\,\mathrm{eV/\,atom}$, that is proportional to R per unit length. Collapse occurs when the latter term prevails above a certain critical tube radii R_{c} that increases with increasing number N of shells of the nanotube. For example: $R_{\mathrm{c}}(N=1) \sim 8d_{\mathrm{vdW}}$ and $R_{\mathrm{c}}(N=8) \sim 19d_{\mathrm{vdW}}$ [13]. The thickness of the collapsed strip-ribbon is obviously $(2N-1)d_{\mathrm{vdW}}$. Any torsional strain imposed on a tube by the experimental environment favors flattening [55,75,76] and facilitates the collapse. The twisting and collapse of a nanotube brings important changes to its electrical properties. For example, a metallic armchair nanotube opens up a gap and becomes a semiconductor as shown in Fig. 21.

6   Summary: Nanomechanics at a Glance

In summary, it seems useful to highlight the 'nanomechanics at a glance', based on the knowledge accumulated up-to-date, and omitting technical details and uncertainties. Carbon nanotubes demonstrate very high stiffness to an axial load or a bending of small amplitude, which translates to the record-high efficient linear-elastic moduli. At larger strains, the nanotubes (especially, the single-walled type) are prone to buckling, kink forming and collapse, due to the hollow shell-like structure. These abrupt changes (bifurcations) manifest themselves as singularities in the non-linear stress-strain curve, but are reversible and involve no bond-breaking or atomic rearrangements. This resilience corresponds, quantitatively, to a very small sub-angstrom effective thickness of the constituent graphitic shells. Irreversible yield of nanotubes begins at extremely high deformation (from several to dozens percent of in-plane strain, depending on the strain rate) and high
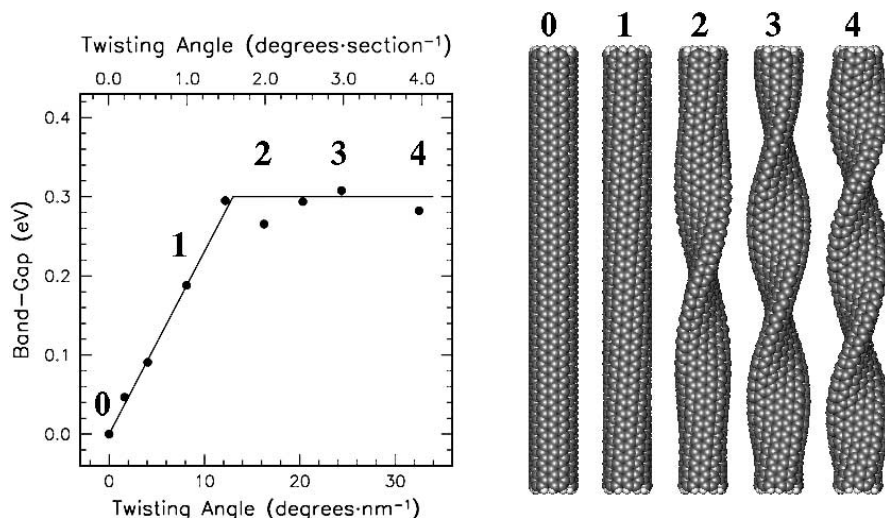
Fig. 21. *Right:* Relaxed structures of a (6,6) nanotube computed using molecular mechanics as a function of the twisting angle. *Left:* Computed band-gap energy using extended Huckel theory as a function of the twisting angle [55]

temperature. The atomic relaxation begins with the edge dislocation dipole nucleation, which (in case of carbon) involves a diatomic interchange, i.e. a ninety-degree bond rotation. A sequence of similar diatomic steps ultimately leads to failure of the nanotube filament. The failure threshold (yield strength) turns out to depend explicitly on nanotube helicity, which demonstrates again the profound role of symmetry for the physical properties, either electrical conductivity or mechanical strength. Finally, the manifestation of mechanical strength in the multiwalled or bundled nanotubes (ropes) is obscured by the poor load transfer from the exterior to the core of such larger structure. This must lead to lower apparent strength and even lower linear moduli, as they become limited by the weak lateral interaction between the tubules rather than by their intrinsic carbon bond network. The ultimate strength of nanotubes and their ensembles is an issue that requires the modeling of inherently mesoscopic phenomena, such as plasticity and fracture, on a microscopic, atomistic level, and constitutes a challenge from the theoretical as well as experimental points of view.

Acknowledgements

References

1. G. Adams, O. Sankey, J. Page, M. O'Keeffe, D. Drabold, Science **256**, 1792 (1992) 302, 305, 307

2. H. G. Allen, P. S. Bulson: *Background to Buckling* (McGraw-Hill, London 1980) p. 582 303

3. M. F. Ashby, Acta. Met. **37**, 1273 (1989) 290

4. Ph. Avouris, Hertel, T., Martel, R., Schmidt, T., Shea, H. R., Walkup, R. E., Appl. Surf. Sci. **141**, 201 (1999) 318, 319, 320, 321

5. F. Banhart, P. M. Ajayan, Nature **382**, 433 (1996) 299, 310

6. R. D. Beck, P. S. John, M. M. Alvarez, F. Diederich, R. L. Whetten, J. Phys. Chem. **95**, 8402 (1991) 287

7. X. Blase, A. Rubio, S. G. Louie, M. L. Cohen, Europhys. Lett. **28**, 335 (1994) 302, 307

8. J. W. Bryson, S. F. Betz, H. S. Lu, D. J. Suich, H. X. Zhou, K. T. O'Neil, W. F. DeGrado, Science **270**, 935 (1995) 321

9. M. Buongiorno-Nardelli, B. I. Yakobson, J. Bernholc, Phys. Rev. Lett. **81**, 4656 (1998) 310, 312, 314, 315, 316

10. M. Buongiorno-Nardelli, B. I. Yakobson, J. Bernholc, Phys. Rev. B **57**, 4277 (1998) 310, 312, 314, 315, 316

11. J.-C. Charlier, T. W. Ebbesen, P. Lambin, Phys. Rev. B **53**, 11108 (1996) 314

12. L. Chico, V. H. Crespi, L. X. Benedict, S. G. Loui, M. L. Cohen, Phys. Rev. Lett. **76**, 971 (1996) 313, 314

13. N. G. Chopra, L. X. Benedict, V. H. Crespi, M. L. Cohen, S. G. Louie, A. Zettl, Nature **377**, 135 (1995) 296, 307, 308, 323

14. N. G. Chopra, A. Zettl, Solid State Commun. **105**, 297 (1998) 293

15. P. G. Collins, A. Zettl, H. Bando, A. Thess, R. E. Smalley, Science **278**, 100 (1997) 314

16. C. F. Cornwell, L. T. Wille, Solid State Commun. **101**, 555 (1997) 303, 307

17. H. Dai, J. H. Hafner, A. G. Rinzler, D. T. Colbert, R. E. Smalley, Nature **384**, 147 (1996) 296

18. P. Delaney, H. J. Choi, J. Ihm, S. G. Louie, M. L. Cohen, Nature (London), **391**, 466 (1998) 320

19. J. F. Despres, E. Daguerre, K. Lafdi, Carbon **33**, 87 (1995) 294, 295

20. M. S. Dresselhaus, G. Dresselhaus, P. C. Eklund, *Science of Fullerenes and Carbon Nanotubes* (Academic, San Diego 1996) p. 965 310, 311

21. M. S. Dresselhaus, G. Dresselhaus, K. Sugihara, I. L. Spain, H. A. Goldberg, *Graphite Fibers and Filaments* (Springer, Berlin, Heidelberg 1988) p. 382 311

22. T. W. Ebbesen, H. Hiura, Adv. Mater. **7**, 582 (1995) 295

23. M. R. Falvo, G. J. Clary, R. M. Taylor, V. Chi, F. P. Brooks, S. Washburn, R. Superfine, Nature **389**, 582 (1997) 296, 297, 320

24. M. S. Fuhrer, J. Nygard, L. Shih, M. Forero, Y.-G. Yoon, M. S. C. Mazzoni, H. J. Choi, J. Ihm, S. G. Louie, A. Zettl, P. L. McEuen, Science, **288**, 494 (2000) 318

25. A. Garg, J. Han, S. B. Sinnott, Phys. Rev. Lett. **81**, 2260 (1998) 303, 307

26. A. Garg, S. B. Sinnott, Phys. Rev. B **60**, 13786 (1999) 308

27. R. C. Haddon, Science **261**, 1545 (1993) 296

28. E. Hernández, C. Goze, P. Bernier A. Rubio, Phys. Rev. Lett. **80**, 4502 (1998) 300, 307

29. E. Hernández, C. Goze, P. Bernier, A. Rubio, Appl. Phys. A **68**, 287 (1999)
    300
30. T. Hertel, R. Martel, Ph. Avouris, J. Phys. Chem. B **102**, 910 (1998)   296,
    317, 320
31. T. Hertel, R. E. Walkup, Ph. Avouris, Phys. Rev. B **58**, 13870 (1998)   317,
    318, 319
32. J. P. Hirth, J. Lothe, *Theory of Dislocations* (Wiley, New York 1982) p. 857
    290, 310
33. H. Hiura, T. W. Ebbesen, J. Fujita, K. Tanigaki, T. Takada, Nature **367**, 148
    (1994)   296
34. S. Iijima, C. Brabec, A. Maiti, J. Bernholc, J. Chem. Phys. **104**, 2089 (1996)
    294, 295, 296, 297, 303, 306, 319, 320
35. C. L. Kane, E. J. Mele, Phys. Rev. Lett. **78**, 1932 (1997)   320
36. B. T. Kelly, *Physics of Graphite* (Applied Science Publishers, London 1981) p.
    478   291, 305, 311
37. V. V. Kozey, H. Jiang, V. R. Mehta, S. Kumar, J. Mater. Res. **10**, 1044 (1995)
    291
38. A. Krishnan, E. Dujardin, T. W. Ebbesen, P. N. Yanilos, M. M. J. Treacy,
    Phys. Rev. B **58**, 14013 (1998)   292, 293, 301
39. L. D. Landau, E. M. Lifshitz: *Theory of Elasticity* (Pergamon, Oxford 1986)
    303, 305, 320
40. J. Liu, H. Dai, J. H. Hafner, D. T. Colbert, R. E. Smalley, S. J. Tans, C. Dekker,
    Nature (London) **385**, 780 (1997)   321
41. O. Lourie, D. M. Cox, H. D. Wagner, Phys. Rev. Lett. **81**, 1638 (1998)   294,
    297
42. J. P. Lu, Phys. Rev. Lett. **79**, 1297 (1997)   300
43. R. Martel, T. Schmidt, H. R: Shea, T. Hertel, Ph. Avouris, Appl. Phys. Lett. **73**,
    2447 (1998)   323
44. R. Martel, H. R. Shea, Ph. Avouris, Nature (London) **398**, 582 (1999)   321,
    322
45. R. Martel, H. R. Shea, Ph. Avouris, J. Phys. Chem. B **103**, 7551 (1999)   321,
    322
46. Y. Miyamoto, A. Rubio, S. G. Louie, M. L. Cohen, Phys. Rev. B **50**, 4976
    (1994)   302
47. Y. Miyamoto, A. Rubio, S. G. Louie, M. L. Cohen, Phys. Rev. B **50**, 18360
    (1994)   302
48. J. Muster, M. Burghard, S. Roth, G. S. Dusberg, E. Hernandez, A. Rubio, J.
    Vac. Sci. Technol. **16**, 2796 (1998)   294, 301
49. G. Overney, W. Zhong, D. Tománek, Z. Phys. D **27**, 93 (1993)   299
50. A. C. Palmer, J. H. Martin, Nature **254**, 46 (1975)   308
51. D. Pierson, C. Richardson, B. I. Yakobson, 6th Foresight Conference on Molec-
    ular Nanotechnology, Santa Clara, CA, http:// www.foresight.org /Conferences
    (1998)   310
52. P. Poncharal, Z. L. Wang, D. Ugarte, W. A. de Heer, Science **283**, 1513 (1999)
    294, 295
53. A. G. Rinzler, J. H. Hafner, P. Nikolaev, L. Lou, S. G. Kim, D. Tománek,
    P. Nordlander, D. T. Colbert, R. E. Smalley, Science **269**, 1550 (1995)   310
54. D. H. Robertson, D. W. Brenner, J. W. Mintmire, Phys. Rev. B **45**, 12592
    (1992)   300, 301, 305

55. A. Rochefort, Ph. Avouris, F. Lesage, D. R. Salahub, Phys. Rev. B **60**, 13824 (1999) 320, 323, 324
56. A. Rubio, J. L. Corkill, M. L. Cohen, Phys. Rev. B **49**, 5081 (1994) 302
57. A. Rubio, Cond. Matter News **6**, 6 (1997) 307
58. R. S. Ruoff, D. C. Lorents, Bull. APS **40**, 173 (1995) 294
59. R. S. Ruoff, J. Tersoff, D. C. Lorents, S. Subramoney, B. Chan, Nature **364**, 514 (1993) 295
60. J. P. Salvetat, G. A. D. Briggs, J. M. Bonard, R. R. Bacsa, A. J. Kulik, T. Stöckli, N. A. Burnham, L. Forro, Phys. Rev. Lett. **82**, 944 (1999) 293, 298
61. D. Sánchez-Portal, E. Artacho, J. M. Soler, A. Rubio, P. Ordejón, Phys. Rev. B **59**, 12678 (1999) 300, 301
62. R. E. Smalley, B. I. Yakobson, Solid State Commun. **107**, 597 (1998) 291, 296, 310
63. D. Srivastava, M. Menon, K. Cho, Phys. Rev. Lett. **83**, 2973 (1999) 303
64. P. Stumm, R. S. Ruoff, B. I. Yakobson (unpublished, 2000) 310
65. B. G. Sumpter, D. W. Noid, J. Chem. Phys. **102**, 6619 (1995) 303
66. K. S. Suslick, (Ed.), *Ultrasound: Its Chemical Physical and Biological Effects* (VCH, Weinheim 1988) 322, 323
67. M. Terrones, H. Terrones, Fullerene Sci. Technol. **4**, 517 (1996) 311
68. J. Tersoff, R. S. Ruoff, Phys. Rev. Lett. **73**, 676 (1994) 295, 308, 320
69. A. Thess, R. Lee, P. Nikolaev, H. Dai, P. Petit, J. Robert, C. Xu, Y. H. Lee, S. G. Kim, A. G. Rinzler, D. T. Colbert, G. E. Scuseria, D. Tománek, J. E. Fischer, R. E. Smalley, Science **273**, 483 (1996) 317, 320
70. S. P. Timoshenko, J. M. Gere, *Theory of Elastic Stability* (McGraw-Hill, New York 1998) p. 541 303, 305
71. M. M. J. Treacy, Ebbesen, T. W., J. M. Gibson, Nature **381**, 678 (1996) 292, 293, 317
72. H. D. Wagner, O. Lourie, Y. Feldman, R. Tenne, Appl. Phys. Lett. **72**, 188 (1998) 298
73. D. A. Walters, Ericson, L. M., Casavant, M. J., Liu, J., Colbert, D. T., Smith, K. A., Smalley, R. E., Appl. Phys. Lett. **74**, 3803 (1999) 298
74. E. W. Wong, P. E. Sheehan, C. M. Lieber, Science **277**, 1971 (1997) 291, 293, 296, 297, 300, 301, 317
75. B. I. Yakobson, C. J. Brabec, J. Bernholc, Phys. Rev. Lett. **76**, 2511 (1996) 300, 303, 304, 305, 308, 323
76. B. I. Yakobson, C. J. Brabec, J. Bernholc, J. Computer-Aided Materials Design **3**, 173 (1996) 296, 300, 303, 307, 308, 323
77. B. I. Yakobson, M. P. Campbell, C. J. Brabec, J. Bernholc, Comput. Mater. Sci. **8**, 341 (1997) 308, 309
78. B. I. Yakobson, R. E. Smalley, American Scientist **85**, 324 (1997) 303, 308
79. B. I. Yakobson, *Fullerenes* (Electrochem. Soc., Paris; ECS, Pennington 1997) p. 549 296, 310, 312, 316
80. B. I. Yakobson, Physical Property Modification of Nanotubes, U. S. Patent Application 60/064,539 (1997) 310, 312, 316
81. B. I. Yakobson, Appl. Phys. Lett. **72**, 918 (1998) 310, 312, 313, 316
82. B. I. Yakobson, G. Samsonidze, G. G. Samsonidze, *Carbon* **38**, 1675 (2000) 317
83. M. Yu, B. I. Yakobson, R. S. Ruoff, *J. Phys. Chem. B Lett.* **104**, 8764 (2000)
84. Yu, M., O. Lourie, M. Dyer, K. Moloni, T. Kelly, R. S. Ruoff, Science **287**, 637 (2000) 298, 299
85. P. Zhang, P. E. Lammert, V. H. Crespi, Phys. Rev. Lett. **81**, 5346 (1998) 310